Hydrodynamic and biochemical impacts on the development of hypoxia in the Louisiana–Texas shelf Part 1: numerical modeling and hypoxia mechanisms

Yanda Ou[1] and Z. George Xue[1,2,3]

[1]Department of Oceanography and Coastal Sciences, Louisiana State University, Baton Rouge, LA, 70803, USA.
[2]Center for Computation and Technology, Louisiana State University, Baton Rouge, LA, 70803, USA.
[3]Coastal Studies Institute, Louisiana State University, Baton Rouge, LA, 70803, USA

Correspondence to: Z. George Xue (zxue@lsu.edu)

Abstract. A three-dimensional coupled hydrodynamic–biogeochemical model with nitrogen, phosphorus, silica cycles, and multiple phytoplankton and zooplankton functional groups was developed and applied to the Gulf of Mexico to study bottom dissolved oxygen dynamics. A 15-year hindcast was achieved covering the period of 2006–2020. Extensive model validation against in situ data demonstrates that the model was capable of reproducing vertical distributions of dissolved oxygen (DO), spatial distributions of bottom DO concentration as well as its interannual variations. Horizontal advection, vertical advection, vertical diffusion, and sedimentary oxygen consumption (SOC) were found as the major factors modulating summer bottom DO dynamics. SOC contributes 33%–51% of summer bottom DO variability over the nearshore regions. Hydrodynamic impacts on the summer bottom DO are also remarkable as the joint contribution of the advection and vertical diffusion reaches 28%–55% and 51%–59% in nearshore and offshore regions, respectively. Sensitivity experiments were carried out to assess the changes in the size of the hypoxic zone due to riverine nutrient reductions. Results of sensitivity experiments highlighted the nonlinear relationship between the reduction of river nutrients and changes in the size of the hypoxic zone, which can be explained by the complexity of the lower-trophic community (e.g., competition on nutrients, grazing, and predation behaviors) Nutrient reductions would not necessarily lead to a decrease in the size of the hypoxic zone. Instead, due to the interactions among different plankton groups, the hypoxic area could even increase under some nutrient-reduction conditions. A triple riverine nutrient reduction (nitrogen, phosphorus, and silica) of 80% is needed to reach the goal of a 5000 km^2 hypoxic zone.

1 Introduction

The Louisiana–Texas (LaTex) shelf in the northern Gulf of Mexico (nGoM) has one of the most notorious recurring hypoxia in the world (bottom dissolved oxygen (DO) < 2 mg L^{-1}, Rabalais et al., 2002; Rabalais et al., 2007a; Justić and Wang, 2014). Regular mid-summer cruises since 1985 have shown that hypoxia usually first emerges in mid-May and persists through mid-September. The hypoxic zone can cover as big as 23,000 km^2 and has a volume of up to 140 km^3 (Rabalais and Turner, 2019; Rabalais and Baustian, 2020). Sensitivity experiments of hypoxia area reduction to different nutrient reduction strategies by

Fennel and Laurent (2018) suggested that to meet the hypoxic area reduction goal (< 5,000 km^2 in a 5-year running average) set by the Hypoxia Task Force (2008), a dual nutrient strategy with a reduction of 48 % of total nitrogen and inorganic phosphorus would be the most effective way. Although nitrogen is the ultimate limiting nutrient, phosphorus load reduction would also lead to a significant reduction of the hypoxia area (Fennel and Laurent, 2018). Transient phosphorus limitation on the shelf (Laurent et al., 2012; Sylvan et al., 2007) was deemed to be associated with the delayed onset and reduction of the hypoxia area.

Coastal eutrophication in the LaTex shelf leads to a high rate of microbial respiration and depletion of DO (Rabalais et al., 2007b). Incubation studies in the LaTex shelf suggested that SOC accounted for 20±4 % (Murrell and Lehrter, 2011) or 25±5.3 % (McCarthy et al., 2013) of below-pycnocline respiration, nearly 7-fold greater than the corresponding percentage at the water overlying sediments (3.7±0.8 %, McCarthy et al., 2013). The fraction of SOC over the total respiration rate at sediments and overlying water was ~87 % according to the measurements by McCarthy et al. (2013). As mentioned by Fennel et al. (2013), the corresponding SOC fraction reached 60 % when applying the water respiration rates of Murrell and Lehrter (2011) and sediment respiration rates of Rowe et al. (2002). Another numerical study (Yu et al., 2015) also pointed out that in the LaTex shelf, oxygen consumption at the bottom water layer was more associated with SOC rather than water column respiration. As it was commonly accepted that SOC was driven by the abundance of organic matter in the sediment, numerical studies developed SOC schemes following this nature (e.g., Justić and Wang, 2014; Fennel et al., 2006; 2011). For example, the instantaneous remineralization parameterization used by Fennel et al. (2006, 2011) estimated SOC as a function of sediment detritus and phytoplankton. Using this scheme, Große et al. (2019) found that the simulated SOC was supported by Mississippi nitrogen supply (51±9 %), Atchafalaya nitrogen supply (33±9 %), and open-boundary nitrogen supply (16±2 %). However, the instantaneous parameterization tends to underestimate SOC at the peak of blooms yet overestimate SOC once the blooms start. In a realistic environment, there should be a lag between the blooms and the peak SOC (Fennel et al., 2013). Recently, developments of coupled sediment–water models emphasized the importance of sedimentary biochemical processes on the SOC dynamics and evolution of bottom hypoxia in the shelf (Moriarty et al., 2018; Laurent et al., 2016). However, coupled sediment–water models are computationally more expensive than simple parameterization of SOC. Therefore, it is crucial to balance the model efficiency and complexity, especially for long-term hindcasts.

The phytoplankton bloom on the shelf results from both cyanobacteria and diatoms (Wawrik and Paul, 2004; Schaeffer et al., 2012; Chakraborty et al., 2017). Cruises data in the nGoM indicated that diatoms accounted for ~50 to ~65 % (inner-shelf) and ~33 to ~64 % (mid-shelf) of chlorophyll a in winter and spring, and ~30 % to ~46 % (inner-shelf) during summer and fall, respectively (Chakraborty and Lohrenz, 2015). A field survey documented that the biovolume contribution of diatoms to the total phytoplankton could be as high as 80 % and 70 % during the upwelling seasons in 2013 and 2014, respectively (Anglès et al., 2019). In the Mississippi River plume, diatoms were found as the most diverse algal class accounting for over 42 % of all unique genotypes observed (Wawrik and Paul, 2004). The phytoplankton community was highly simplified in previous numerical studies, usually with only one phytoplankton functional group considered (e.g., Fennel et al., 2006, 2011, 2013; Laurent et al., 2012; Justić and Wang, 2014).

In addition to SOC and excess nutrient supply from the rivers, water column stratification also plays an important role in regulating the variability of bottom DO concentration in the LaTex shelf. Strong stratification prohibits ventilation of DO and thus results in reduced DO supply to the bottom water layer (Hetland and DiMarco, 2008; Bianchi et al., 2010; Fennel et al., 2011, 2013, 2016; Justić and Wang, 2014; Wang and Justić, 2009; Feng et al., 2014; Yu et al., 2015; Laurent et al., 2018). On the shelf, the river freshwater plume supported by the Mississippi and the Atchafalaya Rivers introduces buoyancy, leading to a stable water column and weak DO ventilation processes (Mattern et al., 2013; Fennel and Testa, 2019). Due to the different distances from major river mouths, the influence of freshwater-induced buoyancy would vary along the shelf. Moreover, the transports and deposition processes of organic matter are affected by the coastal along-shore current systems resulting in different SOC gradients across the shelf. For instance, Hetland and DiMarco (2008) pointed out that in the west of Terrebonne Bay where stratification is usually weak, bottom hypoxia is controlled by bottom respiration.

Despite the above efforts, there are still knowledge gaps in our understanding of the mechanism of hypoxia development as well as a feasible way to reduce the size of the hypoxic zone. First of all, the LaTex shelf is a vast water body and the contribution of sedimentary biochemical and hydrodynamics to hypoxia development is location-dependent. Fennel et al. (2016)(Fennel et al., 2016) divided the shelf into six subregions for model validation purposes instead of for quantifying biochemical and hydrodynamic impacts on bottom DO variability in different shelf regions. A recent study by Ruiz Xomchuk et al. (2021) tried to fill such a gap by decomposing the oxygen equation and found that advection and sediment oxygen demand were the two main contributors to the oxygen budget. But they focused more on the impacts of the temporal and spatial scales of physical processes on bottom DO variability over the west shelf (between 95°W and 92.5°W). Secondly, existing biogeochemical models (e.g., Hetland and DiMarco, 2008; Fennel et al., 2006, 2011, 2013; Laurent et al., 2012; Laurent and Fennel, 2014; Fennel and Laurent, 2018; Justić et al., 2003; Justić et al., 2007; Justić and Wang, 2014; Große et al., 2019; Moriarty et al., 2018) utilized an over-simplified lower-trophic ecosystem (one phytoplankton + one zooplankton function groups or only one phytoplankton group) with one or two embedded nutrient flows (nitrogen or nitrogen+phosphorus). These models could not differentiate the contribution of different plankton groups or the interaction among them in hypoxia development. The nutrients reduction strategies proposed by existing models (mostly based on nitrogen loads; Scavia et al., 2013; Obenour et al., 2015; Turner et al., 2012; Laurent and Fennel, 2019) may be problematic as bottom DO's responses to decreased nutrient loads may not be linear or quasilinear due to the complexity of the lower trophic community.

In this study, we adapted and modified a coupled physical-biogeochemical model covering the entire Gulf of Mexico (GoM) by introducing the oxygen and phosphorus cycles to the North Pacific Ecosystem Model for Understanding Regional Oceanography (NEMURO, Kishi et al. 2007). The model has two phytoplankton and three zooplankton functional groups for a more comprehensive representation of the plankton community. We also modified the instantaneous remineralization parameterization by adding a conceptual sedimentary organic pool (represented by a sedimentary particulate organic nitrogen pool, PONsed; Fig. 1) to allow the accumulation of organic matter in the sediment. Although the SOC scheme applied is similar to that in Justić and Wang (2014), the sedimentary organic matter pool in our study is supported by a more complex plankton community, including three phytoplankton functional groups and two zooplankton functional groups. The influence of the community complexity can be reflected in the SOC and eventually in the bottom DO variability. Based on a 15-year (2006–2020) numerical hindcast, we aimed to 1) understand the contributions of different factors in hypoxia development in different parts of the LaTex shelf; and 2) assess the outcomes of different riverine nutrient reduction scenarios regarding the reduction of the hypoxic zone. In addition, the daily outputs of physical and biochemical conditions will be used to develop a hypoxia prediction model using machine learning techniques (see an accompanying paper in Part 2). In the following sections, model description and modification, model set-ups, and data availability were given in Section 2 (Methods), followed by extensive model validations (Section 3). The main findings of this study and relevant discussion are presented in Section 4.

2 Methods

2.1 Coupled hydrodynamic–biogeochemical model

We adapted the three-dimensional, free-surface, topography-following community model, the Regional Ocean Model System (ROMS, version 3.7), on the platform of Coupled Ocean–Atmosphere–Wave–Sediment Transport (COAWST) modeling system (Warner et al., 2010) to the GoM (Gulf–COAWST). ROMS solves finite difference approximations of Reynolds Averaged Navier–Stokes equations by applying hydrostatic and Boussinesq approximations with a split explicit time-stepping algorithm (Haidvogel et al., 2000; Shchepetkin and McWilliams, 2005, 2009). The biogeochemical model applied is primarily based on the NEMURO developed by Kishi et al. (2007). NEMURO is a concentration-based, lower-trophic-level ecosystem model developed and parameterized for the North Pacific. The original NEMURO model has 11 concentration-based state variables, including nitrate (NO_3), ammonium (NH_4), small and large phytoplankton biomass (PS and PL), small, large, and predatory zooplankton biomass (ZS, ZL, and ZP), particulate and dissolved organic nitrogen (PON and DON), particulate silica (Opal), and silicic acid ($Si(OH)_4$). NEMURO is known for its capability to distinguish ZS, ZL, and ZP and provides a detailed analysis of the dynamics of different functional groups. It was widely used in studies of plankton biomass on regional scales (Fiechter and Moore 2009; Gomez et al., 2018; Shropshire et al., 2020). The embedded silicon cycle permits the inclusion of a diatom group (i.e., PL), the dominant phytoplankton group in the nGoM.

2.2 Model modification

In a recent effort, Shropshire et al. (2020) adapted and modified NEMURO to the GoM with five structural changes. (1) The grazing pathway of ZL on PS was removed since, in the GoM, the PS group is predominated by cyanobacteria and picoeukaryotes, which are too small for direct feeding by most mesozooplankton (i.e., PL). (2) Linear function of mortality was applied for PS, PL, ZS, and ZL, while quadratic mortality was used for ZP, accounting for predation pressure of unmodeled predators, like planktivorous fish. (3) The ammonium inhibition term in nitrate limitation function was no longer considered exponentially but followed the parameterization by Parker (1993). (4) Light limitation on photosynthesis was replaced with Platt et al.'s (1980) functional form, which was also implemented in the newer version of NEMURO. (5) Constant C: Chl ratio was replaced with a variable C: Chl model according to the formulation by Li et al. (2010).

However, neither the modified (Shropshire et al., 2020) nor the original (Kishi et al., 2007) NEMURO model considered phosphorus and oxygen cycles. In this study, we introduced a phosphorus cycle into NEMURO, including three concentration-based state variables as phosphate (PO_4), particulate organic phosphorus (POP), and dissolved organic phosphorus (DOP). The phosphate limitation on phytoplankton growth was introduced using the Michaelis–Menten formula. In the NEMURO model, nitrogen serves as the common "currency", while phosphorus and silicon are converted to nitrogen using the Redfield ratio of P: N: Si=1: 16: 16. In the river-dominated LaTex shelf, inorganic and organic nutrients are supplied mainly by rivers. In our model, riverine PO_4 (Fig. C1), DOP, and POP were prescribed based on water quality measurements at river gages. When no measurement was available, the PO_4, DOP, and POP were approximated using total nitrate+nitrite (NO_3+NO_2), dissolved organic nitrogen (DON), and particulate organic nitrogen (PON) measurements, respectively, via the Redfield ratio of P: N=1: 16. We neglected the POP settling process but preserved these pools by introducing the stoichiometric ratio between phosphorus and nitrogen instead. In other words, the sinking process of POP was implicitly included by building linkages between PON and POP concentrations, as the sinking of PON was considered in the model. Governing equations for phosphorus state variables were given according to Equations 1–3. Please also refer to the appendices for more details on expressions of modified terms (Appendix A), state variables (Appendix Table B1), source and sink terms (Appendix Table B2), and values of parameters (Appendix Table B4).

$$\begin{aligned}\frac{d(PO_4)}{dt} &= (ResPSn + ResPLn)\cdot RPO4N \\ &+(DecP2N + DecD2N)\cdot RPO4N \\ &+(ExcZSn + ExcZLn + ExcZPn)\cdot RPO4N \\ &-(GppPSn + GppPLn)\cdot RPO4N, \end{aligned} \tag{1}$$

$$\begin{aligned}\frac{d(DOP)}{dt} &= (DecP2D - DecD2N)\cdot RPO4N \\ &+(ExcPSn + ExcPLn)\cdot RPO4N, \end{aligned} \tag{2}$$

$$\begin{aligned}\frac{d(POP)}{dt} &= (MorPSn + MorPLn + MorZSn + MorZLn + MorZPn)\cdot RPO4N \\ &+(EgeZSn + EgeZLn + EgeZPn)\cdot RPO4N \\ &-(DecP2N + DecP2D)\cdot RPO4N, \end{aligned} \tag{3}$$

We further adapted the oxygen cycle developed by Fennel et al. (2006, 2013) to NEMURO for hypoxia simulations. However, our model's biochemical dynamics of oxygen are slightly different due to the different plankton functional groups considered. Biochemical sources for oxygen are contributed by photosynthesis of two phytoplankton functional groups, while the sinks are attributed to respirations of two phytoplankton functional groups, metabolism of three zooplankton functional groups, light-dependent nitrification (Olson, 1981; Fennel et al., 2006), aerobic decomposition of particulate and dissolved organic matter (measured as PON, and DON, respectively), and SOC. Wanninkhof's (1992) parameterization was implemented for estimates of oxygen air–sea flux. The biochemical dynamics of oxygen were adopted as follows (see detailed descriptions of variables and parameters in Appendix A–B):

$$
\begin{aligned}
\frac{d(Oxyg)}{dt} = & (rOxNO_3 \cdot GppNPS + rOxNH_4 \cdot GppAPS) \\
& +(rOxNO_3 \cdot GppNPL + rOxNH_4 \cdot GppAPL) \\
& - ResPSn \cdot [RnewS \cdot rOxNO_3 + (1 - RnewS) \cdot rOxNH_4] \\
& -ResPLn \cdot [RnewL \cdot rOxNO_3 + (1 - RnewL) \cdot rOxNH_4] \\
& -rOxNH_4 \cdot (ExcZSn + ExcZLn + ExcZPn) \\
& -2 \cdot Nit \cdot LgtlimN \cdot \hat{r} \\
& -rOxNH_4 \cdot DecD2N \cdot \hat{r} \\
& -SOC \cdot THK_{bot},
\end{aligned} \tag{4}
$$

A sedimentary particulate organic nitrogen (PON_{sed}) pool due to vertical sinking processes of PON was introduced for parameterization of SOC. The SOC scheme (Fennel et al., 2006) is known as the instantaneous consumption of DO. As soon as the PON falls into the sediment bed, PON will be decomposed instantaneously. This scheme tends to underestimate SOC at the peak of blooms and to overestimate SOC after blooms since the lag in SOC demand is neglected (Fennel et al., 2013). We considered such temporal delays in SOC by introducing a PON_{sed} pool. A portion of sinking PON ends up with PON_{sed}, while the rest is buried (PON_{burial}) and is removed from the system. The parameterization is shown in the following. 1) Organic matter settling down at the conceptual sediment layer is remineralized at a temperature-dependent aerobic remineralization rate, K_{P2N}. 2) Sediment oxygen is consumed only in the oxidation of sedimentary organic matter (represented by PON_{sed}) and the nitrification of ammonium to nitrate (Fennel et al., 2006). 3) Oxygen consumption at the conceptual sediment layer directly contributes to oxygen concentration decreases only at the overlying water or bottom water column. Here, we did not distinguish the overlying water and bottom water column since no dynamic sediment module was considered. 4) Sediment denitrification is linearly related to SOC according to observational-based estimates by Seitzinger and Giblin (1996), but the relationship was modified by Fennel et al. (2006) with a slightly smaller slope of denitrification on SOC rate, i.e.,

$$denitrification\ (mmolN\ m^{-2}\ day^{-1}) = 0.105 \times SOC(mmolO_2\ m^{-2}\ day^{-1}), \tag{5}$$

5) Aerobic decomposition of PON_{sed} , sediment nitrification, and denitrification follow chemical equations according to (Fennel et al., 2006):

$$C_{106}H_{263}O_{110}N_{16}P + 106O_2 \leftrightarrow 106CO_2 + 16NH_4 + H_2PO_4 + 122H_2O, \quad \text{(R1)}$$

$$NH_4 + 2O_2 \rightarrow NO_3 + 2H + H_2O, \quad \text{(R2)}$$

$$C_{106}H_{263}O_{110}N_{16}P + 84.8HNO_3 \rightarrow 106CO_2 + 42.4N_2 + 16NH_3 + H_3PO_4 + 148.4H_2O, \quad \text{(R3)}$$

6) Only a portion of NH_4 provided by the aerobic respiration (Eq. (R1)) is used as the source element in the nitrification (Eq. (R2)), while all NO_3 produced by nitrification is used as the source element in denitrification (Eq. (R3)). The linear assumption in 4) implicitly builds relationships among the reactions listed in assumption 5). Let's assume that the production rate of NH_4 by aerobic decomposition (Eq. (R1)) of organic matter is M mmol m^{-3} day^{-1}, and that the fraction of denitrification-produced CO_2 (Eq. (R3)) to the total CO_2 production (Eq. (R1) and (R3)) is x. According to the linear assumption abovementioned, the consumption rate of NO_3 during denitrification (Eq. (R3)) is proportional to the total consumption rate of O_2 in the sediment (Eq. (R1) and (R2)), yielding $\frac{84.8Mx}{16(1-x)} = 0.105 \times \left[\frac{106M}{16} + \frac{84.8Mx}{8(1-x)}\right]$ and further $x \approx 0.1425$. The oxygen consumption rate (Eq. (6)) and organic matter consumption rate (Eq. (7)) due to the coupled aerobic decomposition, nitrification, and denitrification processes can be obtained by substituting the x value into the stoichiometric ratios according to Eq. (R1)–(R3).

$$Oxyg_{consumption} = \frac{106M}{16} + \frac{84.8Mx}{8(1-x)} = 8.3865M, \quad (6)$$

$$OM_{consumption} = \frac{M}{16} + \frac{Mx}{16(1-x)} = 0.0729M, \quad (7)$$

Accordingly, the SOC and consumption rate of PON_{sed} are given, respectively as follows:

$$SOC = Oxyg_{consumption} \cdot THK_{bot} = 8.3865M \cdot THK_{bot}, \quad (8)$$

$$PON_{sed_{consumption}} = 16 \cdot OM_{consumption} \cdot THK_{bot} = 1.1662M \cdot THK_{bot}, \quad (9)$$

where,

$$M = \frac{PON_{sed} \cdot VP2N_0 \cdot exp(K_{P2N} \cdot TMP)}{THK_{bot}}, \quad (10)$$

$$THK_{bot} = thickness\ of\ bottom\ water\ column, \quad (11)$$

For further comparison with the DO concentration, we transferred the SOC rate into a volume-based unit (mg L^{-1} day^{-1}) dividing the rate by THK_{bot}. For simplification, the terminology of SOC was still applied to represent the transferred SOC rate in the following discussion. We further added light inhibition on the nitrification (Olson, 1981) and oxygen dependency on nitrification and aerobic decomposition. These parametrizations were applied following descriptions by Fennel et al. (2006, 2013). For the oxygen-dependent term, an oxygen threshold was specified below which no aerobic respiration or nitrification occurred. Detailed equations were listed in Appendix A. The structure of the newly modified NEMURO model was shown in a schematic diagram in Figure 1.

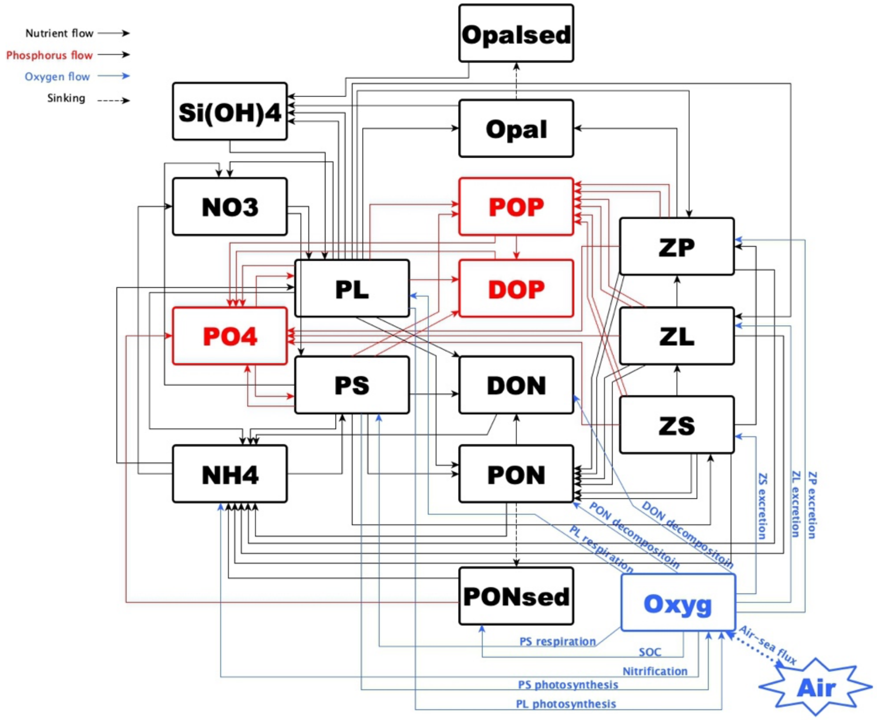

Figure 1. Schematic diagram of the modified NEMURO model. Note that the phosphorus flow and the oxygen flow are two newly added flows to the original NEMURO model.

2.3 Model set-ups

The coupled model was applied to the GoM using Arakawa C-grid with a horizontal resolution of ~5 km (Figure 2a). There are 334 and 357 interior rho points in the east-west and north-south directions, respectively. The model includes 36 sigma layers vertically. The wetting and drying scheme (Warner et al., 2013) was implemented for a more accurate representation of shallow water. The computational time step (i.e., baroclinic time step) was set to 240 seconds while the number of barotropic time steps between each baroclinic time step was set to 30. Model hindcast was carried out from 1 August 2006 to 26 August 2020 with the first 5 months as a spin-up period. Model results were output on a daily interval at UTC 00: 00.

The physical model set-ups largely followed an earlier Gulf–COAWST application (Zang et al., 2018, 2019, 2020). Open boundaries were set at the south and east forced by daily water level, horizontal components of 3-D current velocity, horizontal components of depth-integrated current velocity, 3-D water salinity, and 3-D water temperature derived from the Hybrid Coordinate Ocean Model (HYCOM) global analysis products (Bleck and Boudra, 1981; Bleck, 2002) with data assimilated via the Navy Coupled Ocean Data Assimilation system (Cummings, 2005; Cummings and Smedstad, 2013; Fox et al., 2002; Helber et al., 2013). For lateral boundary conditions, we utilized Chapman implicit for free surface and water level (Chapman, 1985), Flather for depth-integrated momentum (Flather, 1976), gradient for mixing total kinetic energy, and mixed radiation-nudging conditions for 3-D momentum, temperature, and salinity (Marchesiello et al., 2001). The nudging time steps for the mixed radiation-nudging condition were set to 1 day for inflows and 30 days for outflows. The boundary nudging technique was performed at the computational grids along the open boundary. The boundary condition types for passive biochemical tracers (i.e., PS, PL, ZS, ZL, ZP, NO_3, NH_4, PON, DON, $Si(OH)_4$, opal, PO_4, POP, DOP, and Oxyg) were all prescribed as radiation.

Initial conditions for water level, horizontal components of 3-D current velocity, horizontal components of depth-integrated current velocity, 3-D water salinity, and 3-D water temperature were provided by the same HYCOM products as well. Initial conditions for concentrations of NO_3, PO_4, and $Si(OH)_4$ were interpolated from measurements provided by the World Ocean Database (WOD, Boyer et al., 2018). Initial conditions for DO concentration were given by World Ocean Atlas (WOA, Garcia et al., 2018). Other biochemical tracers were initialized as 0.1 mmol m^{-3} due to the lack of observations.

Atmospheric forcings, including surface wind velocity at 10 m height above sea level, net longwave radiation flux, net shortwave radiation flux, precipitation rate, air temperature 2 m above sea level, sea surface air pressure, and relative humidity 2 m above sea level, were derived from the National Centers for Environmental Prediction (NCEP) Climate Forecast System Reanalysis (CFSR) 6-hourly products (for years prior to 2011, Saha et al., 2010) and NCEP CFS Version 2 (CFSv2) 6-hourly products (for years starting from 2011, Saha et al., 2011) with a horizontal resolution of ~35 km and ~22 km, respectively. In our model, 63 rivers were considered as horizontal point source forcings along the coastal GoM. They were split into 280 points (red dots in Fig. 2a) sources transporting time-varying salinity (nearly zero), temperature, 3-D horizontal momentum (based on the magnitude of river discharges), nutrients (NO_3, NH_4, PO_4, $Si(OH)_4$, PON, DON, POP, and DOP; Fig. C1), and DO to the computational domain. Locations of river point sources of the Mississippi and the Atchafalaya Rivers were shown as red dots in Figure 2b. For reconstructions of time series of river forcing terms, we composed measurements from various sources, including U.S. Geological Survey (USGS) National Water Information System (NWIS), National Oceanic and Atmospheric Administration (NOAA) Tides and Currents System (TCS), NOAA National Estuarine Research Reserve System (NERRS), and Mexico National Water Commission (CONAGUA, for rivers in Mexico's territory). Daily averaged river discharges were given based on measurements by USGS NWIS and CONAGUA. The magnitude of river discharges was multiplied by 1.4 to account for adjacent watershed areas and lateral inflow of tributaries (Warner et al., 2005). River temperature and salinity time series were reconstructed from measurements by USGS NWIS, NOAA TCS, and NOAA NERRS. River nutrient concentrations were provided monthly by USGS NWIS and NOAA NERRS and were extended to daily time series with values in the corresponding months. Riverine DO concentration was set to be a constant (258 mmol m^{-3}) assuming that riverine DO was saturated at 25 ℃ under 1 atm. Besides, tidal forcings were introduced in the hydrodynamic model taking into account of influences of tidal elevations and tidal currents. There were 13 tidal constituents considered in the model including M2, S2, N2, K2, K1, O1, P1, Q1, MF, MM, M4, MS4, and MN4.

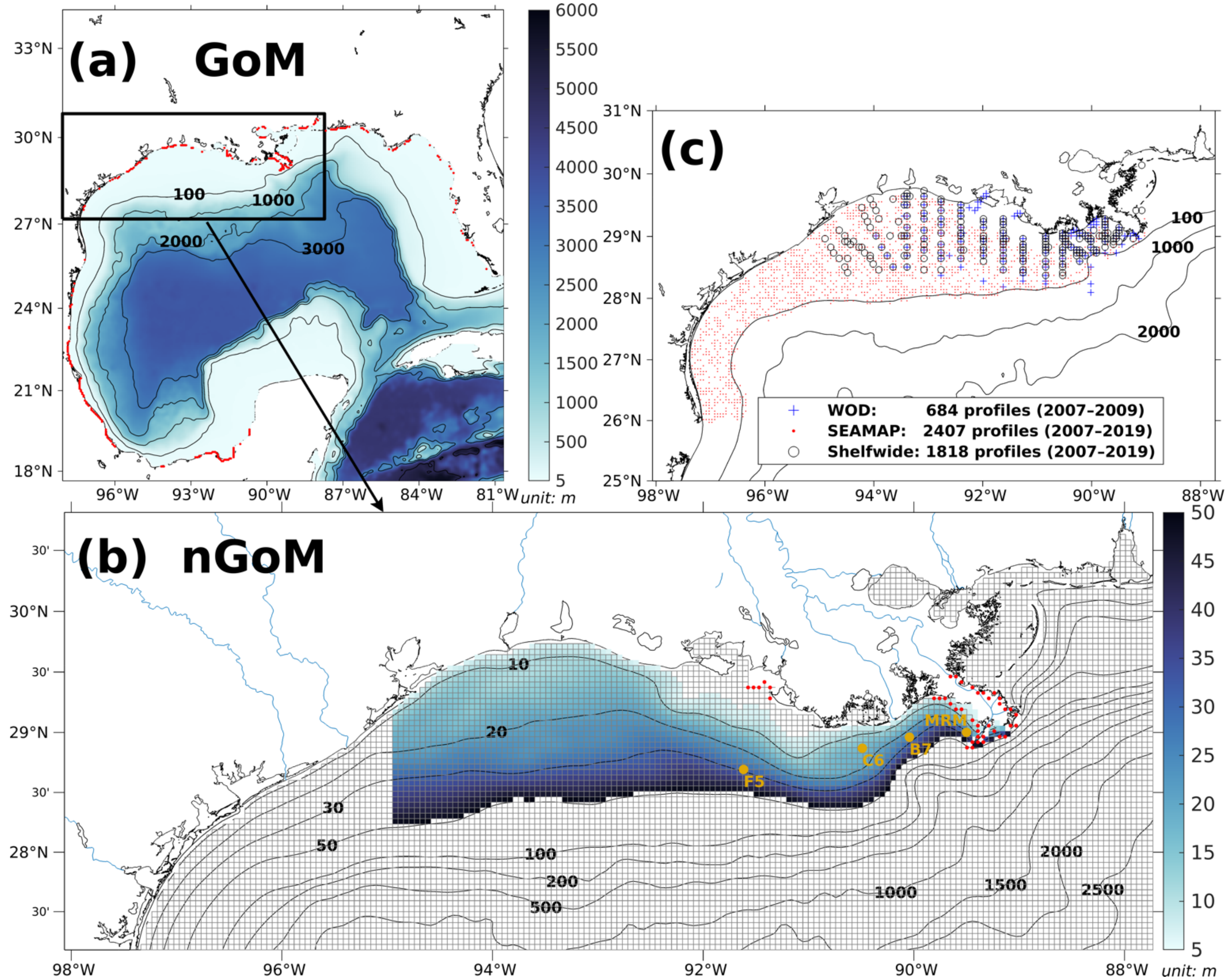

Figure 2. (a) Bathymetry of the entire domain of the Gulf–COAWST, (b) zoom-in bathymetry plot of the northern Gulf of Mexico (nGoM), and (c) locations of observed inorganic nutrient and DO profiles derived from WOD, SEAMAP, and NOAA's shelf-wide cruises. In (a), locations of river point sources are denoted by red dots. In (b), only bathymetry between 6 and 50 m was mapped with colors; computational meshes were split by solid grey lines; main river channels are denoted by solid blue curves; locations of river point sources of the Mississippi and the Atchafalaya rivers are indicated by red dots; sampling locations for SOC and overlaying water respiration measurements by McCarthy et al. (2013) are denoted by dark yellow dots.

3 Biogeochemical model validations

3.1 Available measurements

In this section, biogeochemical model validations were conducted for inorganic nutrient concentration profiles (i.e., NO_3, PO_4, and $Si(OH)_4$), ratios of diatom and total phytoplankton, SOC, ratios of SOC and overlaying water respiration, DO concentration profiles, spatial distributions of bottom DO concentration, and temporal variability of the hypoxic area against multiple data sets derived from cruise measurements and literature. Model simulated profiles were linearly interpolated to depths of the observed profiles for a quantitative comparison. Validation of the hydrodynamic model can be found in Zang et al. (2019).

Inorganic nutrient concentration profiles from WOD were used for model validation. WOD measurements cover the period from 11 January 2007 to 5 July 2009 including 478 NO_3 profiles, 409 PO_4 profiles, and 217 $Si(OH)_4$ profiles. The diatom percentage of total phytoplankton was derived from measurements by Chakraborty and Lohrenz (2015) and Schaeffer et al. (2012). The SOC and overlaying water respiration measurements were from an incubation study (McCarthy et al., 2013). Available DO concentration profiles were obtained from the WOD, NOAA-supported mid-summer shelf-wide cruises, and Summer Groundfish Survey in GoM supported by Southeast Area Monitoring and Assessment Program (SEAMAP) conducted annually by the Gulf States Marine Fisheries Commission. There were 445 DO profiles (11 January 2007 to 5 July 2009) from WOD. The shelf-wide cruises provided 1818 measured profiles with 85140 available records from 2007 to 2019. There were at least 83 DO profiles for each summer (June–August, except 2016) from the shelf-wide cruise observations. The selected SEAMAP DO dataset covers a time range from 2007 to 2019 with measurements including 2407 profiles with 77415 sampled records. Locations of the selected profiles from different archives were shown in Figure 2c. Summer measurements by the shelf-wide cruises were used for the validation of spatial patterns of bottom DO concentration and time series of summer hypoxic areas. Estimated hypoxic areas by the cruises are available from 2007 to 2020 with a range from 5,480 km^2 to 22,720 km^2.

3.2 Nutrients concentration profiles

Modeled results showed good agreements with WOD nutrient profiles (Fig. 3a, 3d, and 3g, averaged every 2 m from the surface to 50 m depth) in terms of vertical patterns and magnitudes. The surface waters were rich in NO_3 (Fig. 3a) but oligotrophic in PO_4 (Fig. 3d) and $Si(OH)_4$ (Fig. 3g), indicating a possibly high diatom productivity (Baronas et al., 2016) and possible phosphorous or silicon limitation in the photic zone. NO_3 concentrations decreased drastically at a depth between 10 and 15 m and were maintained at a low level from 15 to 50 m. A bi-peak structure was found in both PO_4 and $Si(OH)_4$ concentration profiles. The first peak (also the higher ones) of PO_4 concentration occurred at around 10–20 m depth while the second peak was at around 35 m depth as illustrated by the averaged values and corresponding 10–90 percentiles. In contrast, the high peak of $Si(OH)_4$ concentration occurred at around 35 m depth while the low peak at the depth of around 15 m, which is consistent with biogenic silica remineralization at lower water columns (Baronas et al., 2016). The simulated profiles were linearly interpolated to the observed depth for point-to-point comparisons. The probability histograms of concentration differences illustrated that our model generally overestimated NO_3 (Fig. 3b) and PO_4 (Fig. 3e) but underestimated $Si(OH)_4$ (Fig. 3h). About 60% of total NO_3 differences fell within a range from -10 to 10 mmol m^{-3} with 43 % in the positive interval (i.e., from 0 to 10 mmol m^{-3}). The corresponding statistics of PO_4 comparisons within a range of ±0.4 mmol m^{-3} were 53 % (-0.4–0.4 mmol m^{-3}), 31 % (0–0.4 mmol m^{-3}), and 22 % (-0.4–0 mmol m^{-3}), respectively. Approximately 13 % of observed

$Si(OH)_4$ were overestimated within 10 mmol m^{-3} and ~51 % were underestimated within 10 mmol m^{-3}. At surface layers (0–5 m), similar probability patterns in nutrient biases were found but with slightly different statistics (Fig. 3c, 3f, and 3i). For example, about 34 % of NO_3 concentrations were overestimated within 10 mmol m^{-3} compared to 10 % of surface measurements underestimated within 10 mmol m^{-3}. Mean NO_3 concentrations from the Mississippi and the Atchafalaya Rivers were 99 ± 34 mmol m^{-3} (mean ± 1sd) and 66 ± 29 mmol m^{-3}, respectively. Mean riverine PO_4 concentrations were 2.7 ± 0.7 mmol m^{-3} and 2.3 ± 0.7 mmol m^{-3}, respectively, and mean riverine $Si(OH)_4$ concentrations were 118 ± 23 mmol m^{-3} and 116 ± 21 mmol m^{-3}, respectively. The nutrient concentrations bias between simulations and observations is acceptable concerning the strong influences of high riverine nutrient loads on the shelf.

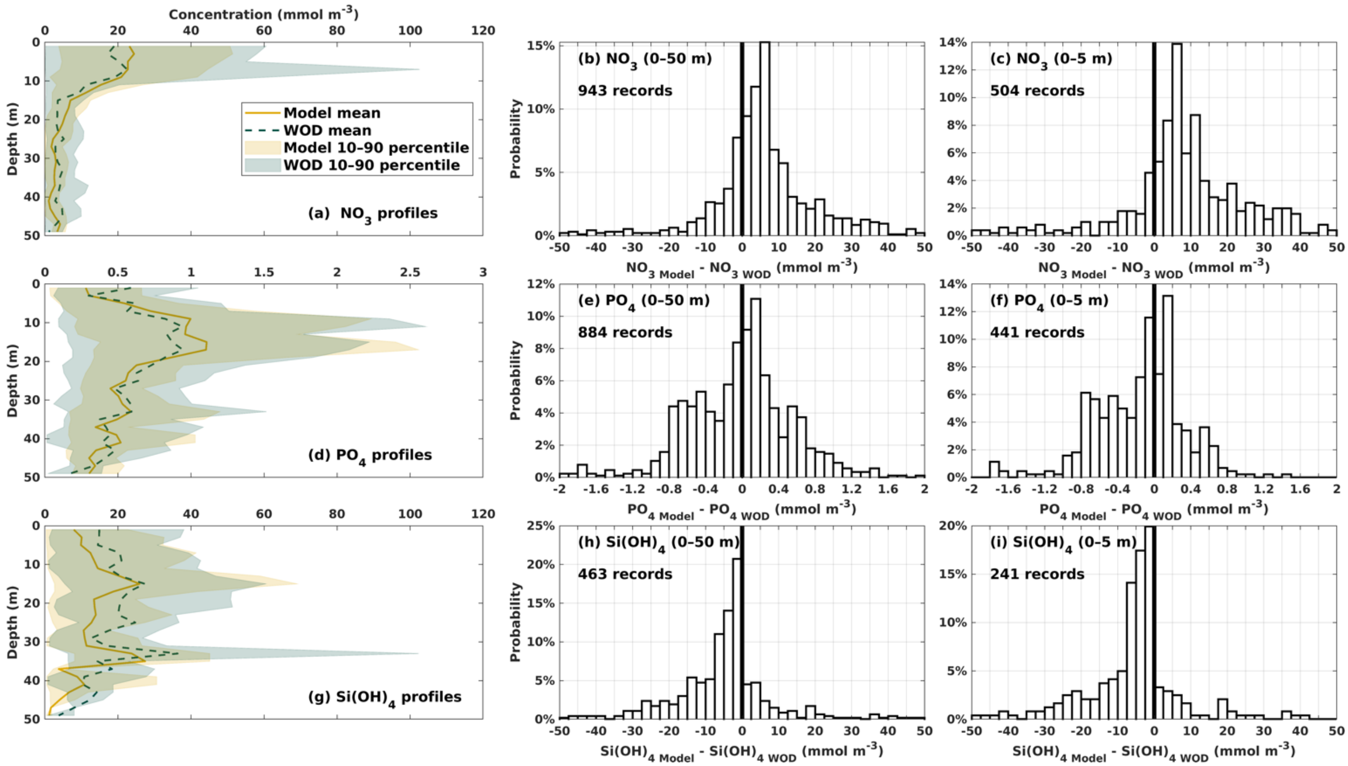

Figure 3. Profile comparisons between model hindcasts and WOD measurements for concentrations of (a)–(c) NO_3, (d)–(f) PO_4, and (g)–(i) $Si(OH)_4$. Note that the thick vertical lines in (b), (c), (e), (f), (h), and (i) denote the concentration difference of 0 separating the positive and negative intervals.

3.3 Diatom ratios

Both measured and model simulated $Si(OH)_4$ profiles suggested strong diatom productivity in the photic zone (Fig. 3g). Cruise observations confirmed that the LaTex phytoplankton community is dominated by the diatom group (Schaeffer et al., 2012; Chakraborty and Lohrenz, 2015). Regional averages (Fig. C2 in Appendix C), vertical averages (only the surface, middle, and bottom layers were chosen), and monthly averages were applied to the concentration ratio of diatom and total phytoplankton according to the sampled locations, sampled layers, and sampled months, respectively, of the cruise studies by Schaeffer et al.

(2012) and Chakraborty and Lohrenz (2015). The modeled ratios well reproduced the measured ones in terms of magnitudes, monthly variability, and cross-shelf variability (Table 1). During the cruise periods in 2008, the range of modeled diatom percentage (79% to 99%) matched well with the measurements (79% to 88%) except for June 2008 when underestimations were found. In 2009, our model results agreed well with the measurements in inner shelf waters but overestimated in the mid-shelf regions, especially in the summer and fall of 2009. The measured percentages exhibited salient monthly variations with higher values in winter and spring and low ones in summer and fall. In the cross-shelf direction, the phytoplankton community shifted from a highly diatom-dominated one in the inner shelf waters to a less diatom-dominated one in the mid-shelf waters, especially in summer. Such patterns were well captured by our model.

Table 1. Comparison of simulated (mean ± 1SD) and measured (mean ± 1SD in parentheses) diatom percentage of the total phytoplankton. Note that the statistics for the simulated percentages were conducted based on concentration values and averaged over the cruise months and over given regions that cover the cruise sampling locations (Fig. C2). The measured percentages by Schaeffer et al. (2012) (for measurements in 2008) were calculated based on biovolume values, while those by Chakraborty and Lohrenz (2015) (for measurements in 2009) were given by chlorophyll *a* attributed to different phytoplankton groups

	Diatom/total phytoplankton × 100%	
	Inner shelf	Midshelf
February 2008	99±4 (88±16)	
April 2008	99±2 (71±16)	
May 2008	79±39 (79±22)	
June 2008	29±42(85±10)	
January 2009	60±29 (66±21)	57±14 (47±14)
April 2009	50±33 (59±14)	51±19 (33±29)
July 2009	41±33 (40±13)	33±24 (13±16)
October–November 2009	50±33 (46±14)	38±19(19±17)
March 2010	49±35 (50±14)	52±26 (64±12)

3.4 SOC and overlaying water respiration

McCarthy et al. (2013) provided incubation measurements of the SOC rates and overlaying water respiration at five shelf water sites (Fig. 1 in McCarthy et al., 2013) using sediment and water samples collected during six cruises (i.e., July 2008, September 2008, January 2009, August 2009, May 2010, and May 2011). Modeled SOC rate and SOC/overlaying water respiration ratio were then compared against the measurements. The modeled overlaying water respiration rate was approximated by the rate calculated at the bottom water column considering biochemical processes that occurred at that layer, i.e., phytoplankton respiration rates, zooplankton metabolism rates, aerobic decomposition rates of PON and DON, and nitrification rate. The modeled SOC and ratio of SOC/overlaying water respiration were averaged over the cruise months for four shelf sites (i.e., F5, C6, B7, and MRM; Fig. 2b). Our model could well capture the SOC magnitude and variability. Both measured and modeled ratios of SOC/ overlaying water respiration were found greater than 1, highlighting the importance of SOC in bottom DO dynamics (Fig. 5). The model generally overestimated the SOC at sites F5 and C6 except for January 2009 and May 2010 at site C6, and underestimated SOC at sites B7 and MRM (Fig. 4). The modeled ratio agreed with the measurements except for site MRM in August 2009. Such a bias might result from the prescription of river inputs along the model boundary for diverting momentum and concentration tracers from the river point sources to the computational grid cells. The scheme could lead to an overshot of fresh water at the near-mouth grid cells and a short residence time for organic matter in the water column and an underestimation of the overlaying water respiration rate. As the model results were averaged over an entire month but not over the exact cruise date due to the lack of cruise information in McCarthy et al. (2013), we considered model-simulated SOC and ratio of SOC/overlaying water respiration acceptable.

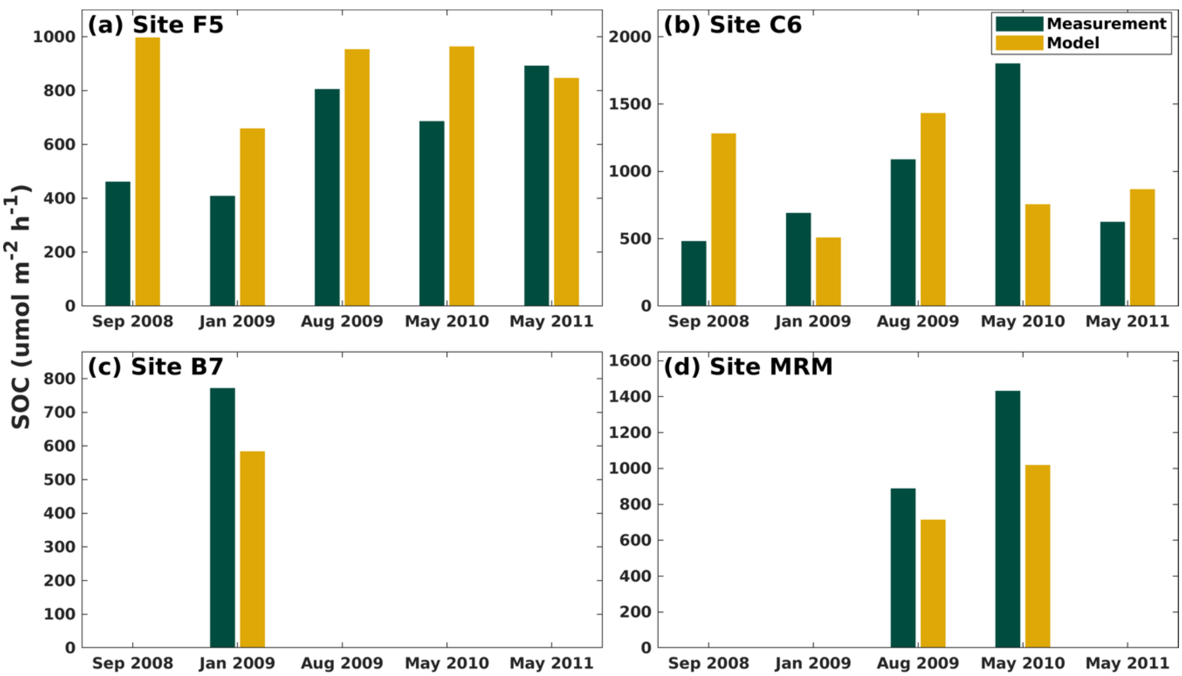

Figure 4. Comparison of modeled and measured SOC (unit: µmol m^{-2} h^{-1}) at four LaTex shelf sites (Fig. 2b). Note that the measurements are provided by McCarthy et al.'s (2013) incubation study.

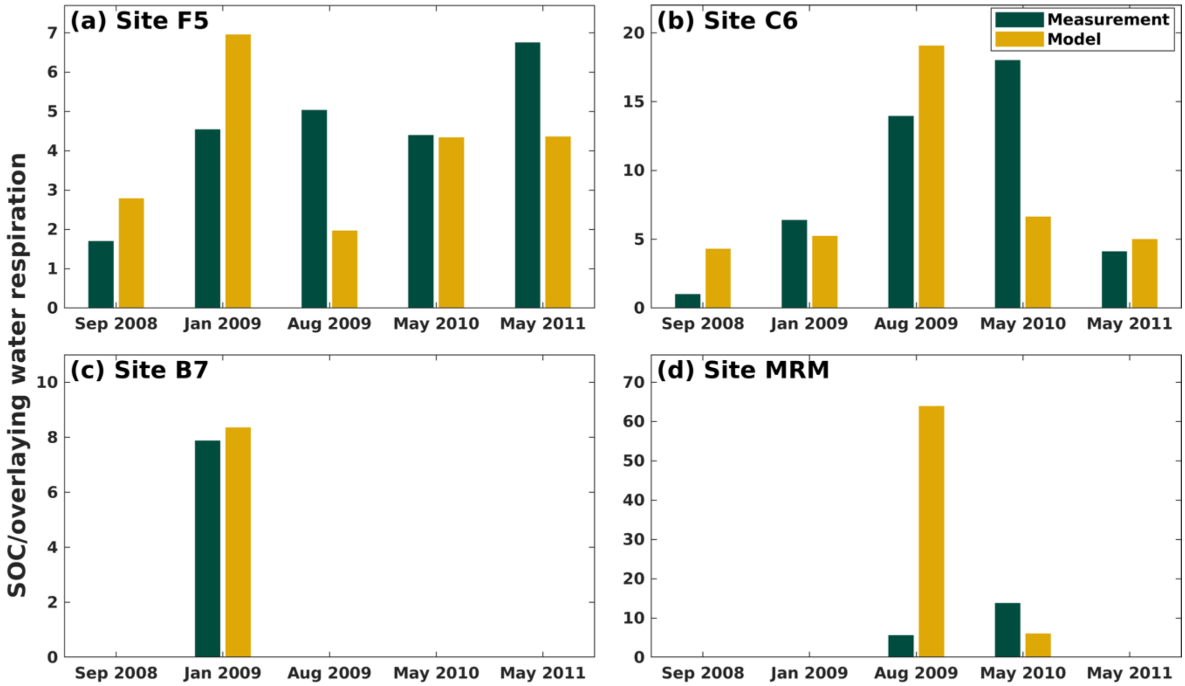

Figure 5. Comparison of modeled and measured (McCarthy et al., 2013) ratios of SOC/overlaying water respiration at four LaTex shelf sites.

3.5 DO profiles

Both simulated and observed DO profiles were averaged every 2 m from the surface to 50 m depth (Fig. 6a, 6c, and 6e). The observed DO vertical structures, such as the "zigzag" shape in the WOD profiles and "C" shape in the shelf-wide and SEAMAP profiles, were well captured by the model. The 10–90 percentile of modeled DO overlap the measured ones. Probability histograms of relative bias between the model and measurements reveal that the model overestimated the measured DO (Fig. 6b, 6d, and 6f). There were 45% (27%) of the WOD DO samples were overestimated (underestimated) by 50%. When compared to the shelf-wide cruise measurements, the probability histogram of the relative bias showed a bell-shaped distribution with a peak around zero. 28 %, 44 %, and 66 % of observations were misestimated by ±10 %, ±20 %, and ±50 %, respectively (Fig. 6d). Our model seemed to agree well with SEAMAP data. There were 36% (20%), 50% (26%), and 61% (31%) of records being overestimated (underestimated) by 10%, 20%, and 50%, respectively (Fig. 6f).

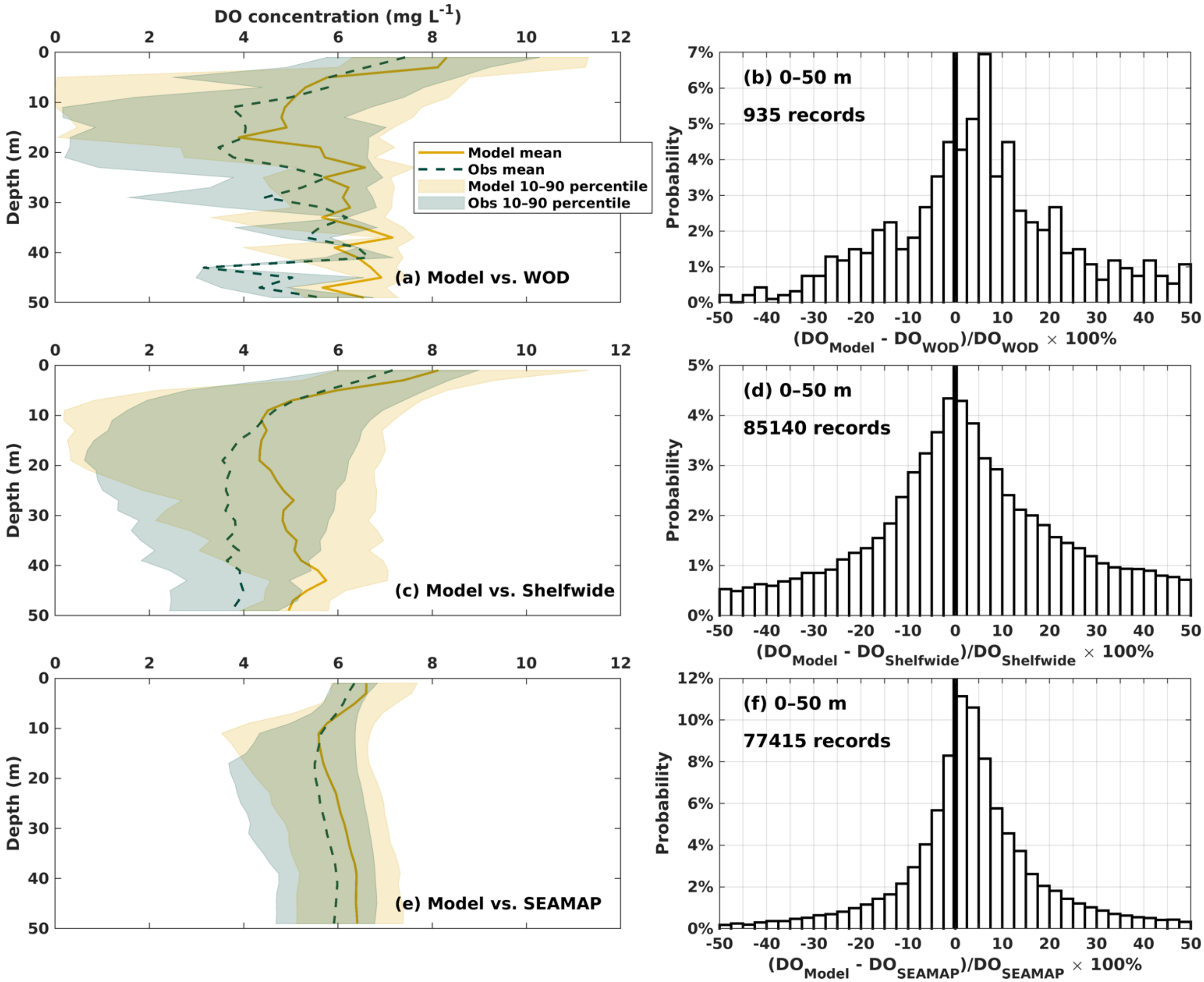

Figure 6. Comparisons of DO profiles between model hindcasts and measurements by (a–b) WOD, (c–d) NOAA's shelf-wide cruises, and (e–f) SEAMAP. Probability histograms of relative percentage differences between modeled and observed DO are in the right column. The thick vertical lines in the histograms denote the percentage difference of 0.

3.6 Spatial distributions of bottom DO and temporal variability of hypoxic area

As the annual NOAA shelf-wide cruises were conducted from the east shelf to the west in the summer, model simulated bottom DO was resampled following the cruise periods. For example, if the westmost location of the cruise is 90°W on day 1, the simulated bottom DO concentration over the east of 90°W on that day is extracted. On the following day, if the westmost location of the cruise is 91°W, the simulation between 91°W and 90°W on day 2 is extracted, and so forth. All the extract frames were blended to reconstruct the spatial distribution of simulated bottom DO concentration during the summer cruise period. Simulated results outside the LaTex shelf and over the deep (> 50 m) and shallow (< 6 m) water regions were excluded since observations were unavailable over these regions. Numerical results showed a good agreement with the observations in terms of interannual variability and spatial extent of bottom hypoxic waters (Fig. 7). The spatial distribution of the hypoxic regions varied over different summers. For example, the hypoxic area was small and was primarily restricted in nearshore (<20 m) regions during the summers of 2007, 2009, 2010, 2012, 2014, and 2018. The size of the hypoxic zone was more prominent and extended offshore in 2008, 2011, 2013, and 2019. The spatial dispersion of hypoxic waters occurred mostly over the west of the LaTex shelf, where bathymetry gradients were gentle. Over the eastern shelf, the hypoxic water was mostly constrained within a narrow belt. In the meantime, the western and eastern hypoxic water was not always merged but were separated at around 91 °W (e.g., 2007, 2010, 2012, 2014, 2017, and 2018). These results suggested that the hypoxia development on the LaTex shelf was complex and generally followed the bathymetry and distances from the major river mouths.

The daily time series of the size of the hypoxic zone was calculated over the LaTex shelf (6–50 m; Fig. 8). There was a good agreement between simulated hypoxia zone size and that captured by the shelf-wide cruises in terms of variability and magnitude. The overall R^2 was found as 0.47 and varied yearly (Table 2). The 5-year running R^2 increased from 0.02 for the first 5-year period (2007–2010) to 0.91 for the last 5-year period (2015–2020, excluding 2016). The poor performance before 2010 could be attributed to the coarse resolution of the atmospheric forcings (~ 35 km) provided by CFSR. Since 2011, CFSRv2 provided forcings with a higher resolution of 22 km. Notable underestimations were found in 2007, 2010, 2012, and 2014 with a root-mean-squared error (RMSE) of 9988 km^2, while minor underestimations were simulated in 2008, 2017, 2018, and 2020 (RMSE=4862 km^2). The model tended to slightly overestimate the measurements in other summers of interest (i.e., 2009, 2011, 2013, 2015, and 2019; RMSE=2132 km^2). Nevertheless, those biases were acceptable considering the relative sporadic converges of cruise data.

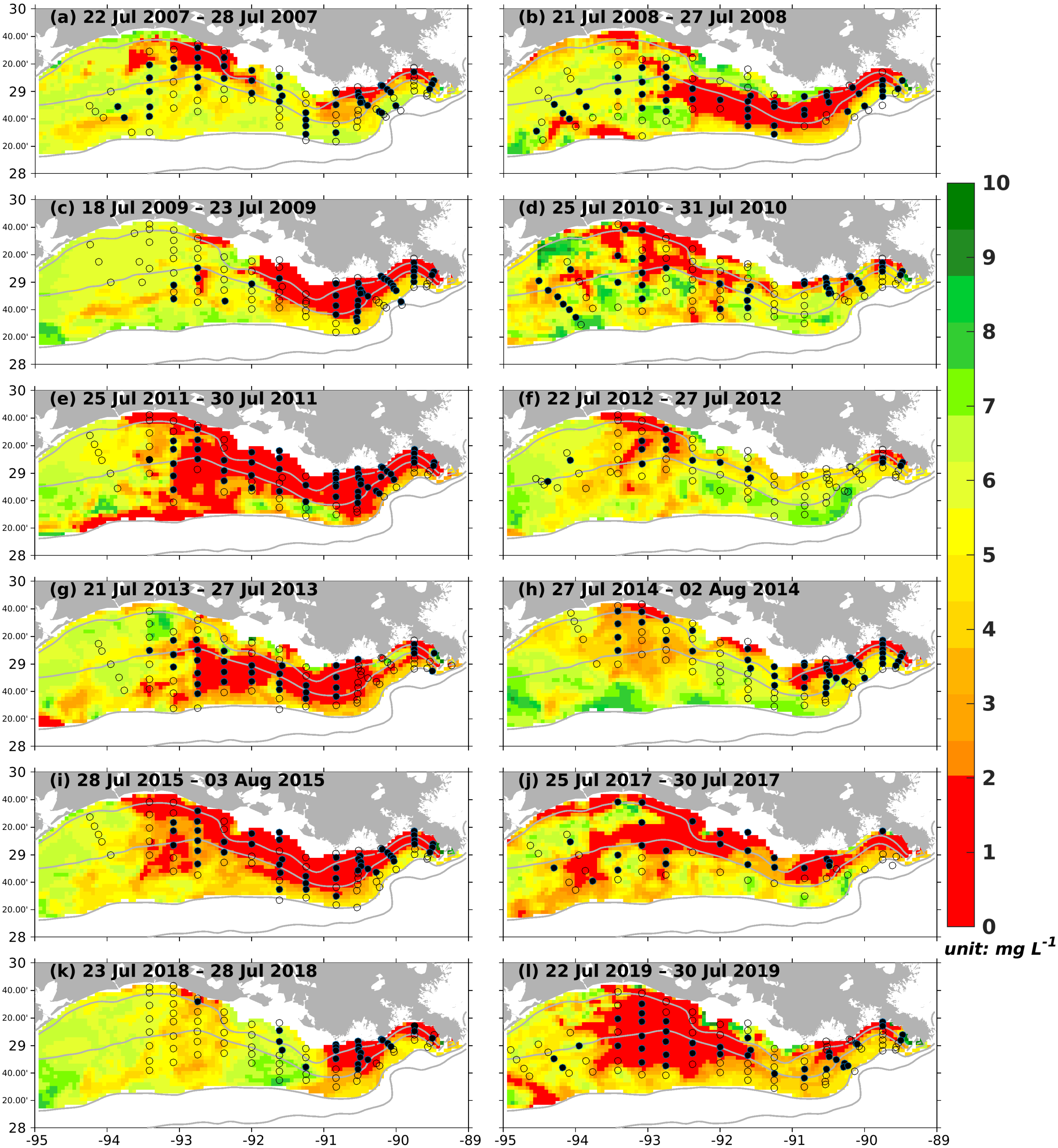

Figure 7. Modeled summer bottom DO concentration (colored patches) and NOAA's summer shelf-wide hypoxia observations (black dots and open circles). The black dots and the open circles are indicators of observed bottom hypoxia and normoxia, respectively. The solid grey lines indicate bathymetry of 10, 20, 50, and 100 m, respectively.

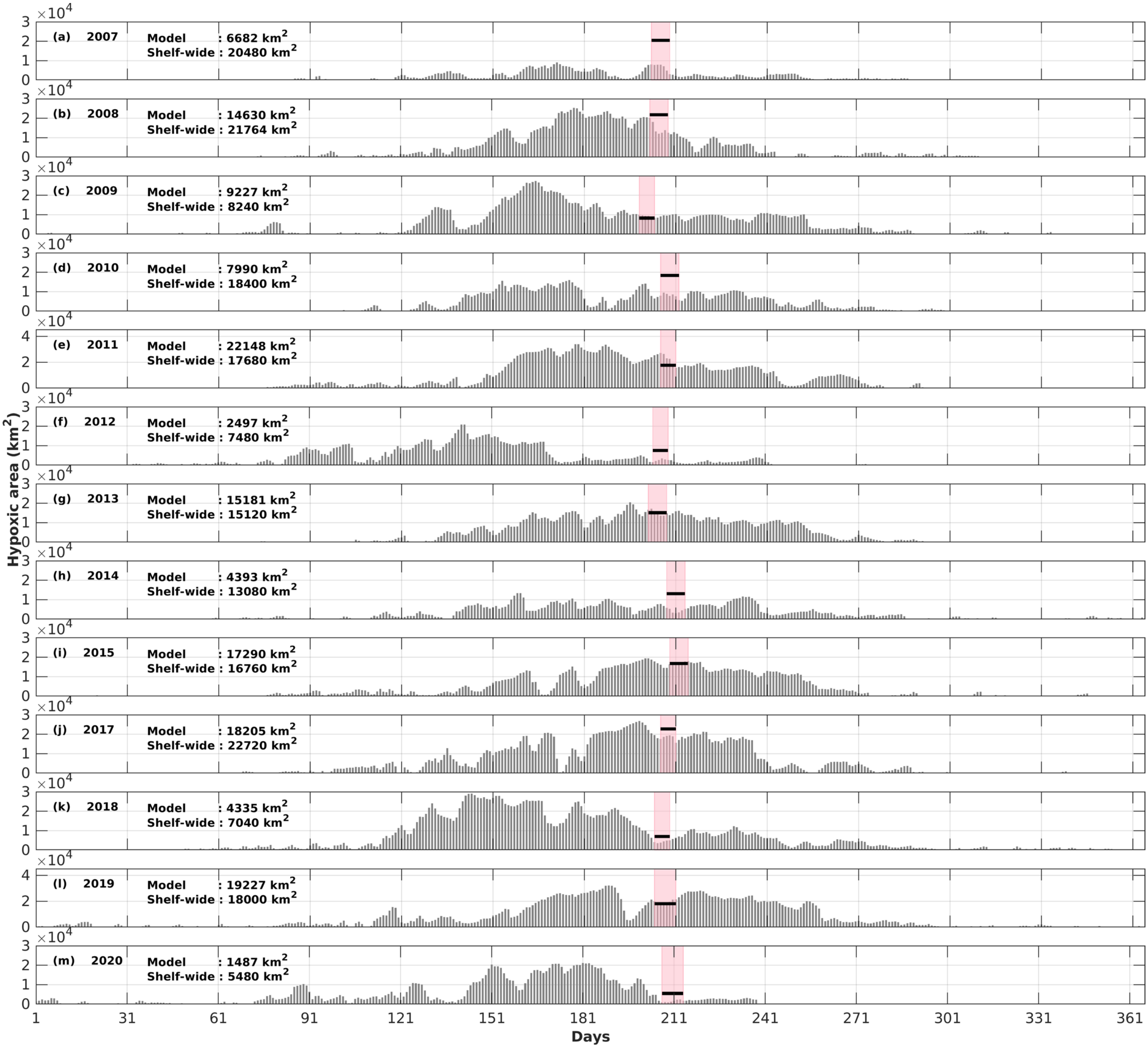

Figure 8. Comparison of the hypoxic area (in km^2) between model simulations and shelf-wide cruise observations from 2007 to 2020 (except 2016). The pink patches denote the cruises periods while the solid black lines represent the measured hypoxic area.

Table 2. The overall (2007–2020) and 5-year running R^2 of summer hypoxic area between model simulations and shelf-wide measurements. Note that the comparison in the year 2016 was excluded due to the lack of measurement.

Year ranges	R2	Year ranges	R2
2007–2020 (overall)	0.47	2011–2015	0.82
2007–2011	0.02	2012–2017	0.75
2008–2012	0.39	2013–2018	0.71
2009–2013	0.41	2014–2019	0.73
2010–2014	0.44	2015–2020	0.91

4 Results and discussion

4.1 Factors controlling subregion bottom DO variability

Fennel et al. (2016)(Fennel et al., 2016) divided the inner shelf (<50 m water depth) into six subregions (Fig. 9a) largely following the bathymetry and distances from the major river mouths: from east to west, two west-Mississippi regions (6–20 m nearshore and 20–50 m offshore regions, similar hereinafter), two mid-Atchafalaya regions, and two west-Atchafalaya regions. Focusing on the bottom DO concentration balance, we calculated five hydrodynamic-related terms (i.e., the local rate of changes in bottom DO, horizontal advection of bottom DO, horizontal diffusion of bottom DO, vertical advection of bottom DO, and vertical diffusion of bottom DO) and two biochemical-related terms (i.e., biochemical-induced changes in DO at the bottom water column, and SOC). The biochemistry at the bottom water column includes processes of phytoplankton photosynthesis, phytoplankton respiration, zooplankton metabolism, aerobic decomposition of PON and DON, and nitrification. The summation of these seven terms contributes directly to the total changes in bottom DO concentration. The contribution of a given term was estimated by the percentage of the corresponding absolute value over the summation of all the absolute terms. We then averaged the absolute percentages over the entire LaTex shelf (water depth 6-50 m) and over the six subregions, respectively.

Monthly climatology illustrated that the variability of bottom DO on the LaTex shelf was mostly controlled by four processes: horizontal advection, vertical advection, vertical diffusion, and SOC (Fig. 9b). The sum of the percentages of contributions from these four terms (absolute values) was more than 80%. The contributions of the two advection terms exhibited a salient seasonal pattern with the maximum in spring and winter and the minimum in summer. The contribution of SOC showed an opposite pattern and reached its peak (34%) in summer. It was interesting to note that no salient seasonal pattern was found in the percentage of contribution from the vertical diffusion term, which maintained around 20% over a year. The vertical diffusion of DO was determined by both vertical DO gradient and vertical stratification. The robust contribution of vertical diffusion highlighted the importance of stratification on bottom DO variability throughout the year. The importance of DO advection and SOC on bottom DO balance was also documented by Ruiz Xomchuk et al. (2021), where, however, vertical diffusion was proposed as a minor contributor. Such a disagreement could result from the water layers investigated. Vertical diffusion of DO across the layer 10 m above the bottom was discussed in Ruiz Xomchuk et al. (2021), while here we estimated vertical diffusion of DO across the bottom layer.

The contributions of the four terms on the bottom DO varied in different subregions. In the nearshore regions (6–20 m; Fig. 9c, 9e, and 9g), SOC played a much more important role than the other three terms in modulating the summer bottom DO concentration. The maximum contribution from SOC was 33%–51% while the contributions of two advection terms were only ~10% or even lower. In contrast, over the offshore regions (20–50 m; Fig. 9d, 9f, and 9h), the contribution of SOC decreased notably to 19%–27% in summer and was comparable to the other three hydrodynamic-related terms (18%–26% for the horizontal advection, 17%–25% for the vertical advection, and 7%–16% for the vertical diffusion). During other months, the bottom DO was mostly modulated by the advection processes in the offshore regions. Similar to the regional mean over the entire shelf, the contribution of vertical diffusion maintained almost the same level over a year in both nearshore and offshore regions. The vertical diffusion term contributed more to the total changes in bottom DO in the nearshore regions than in the offshore regions.

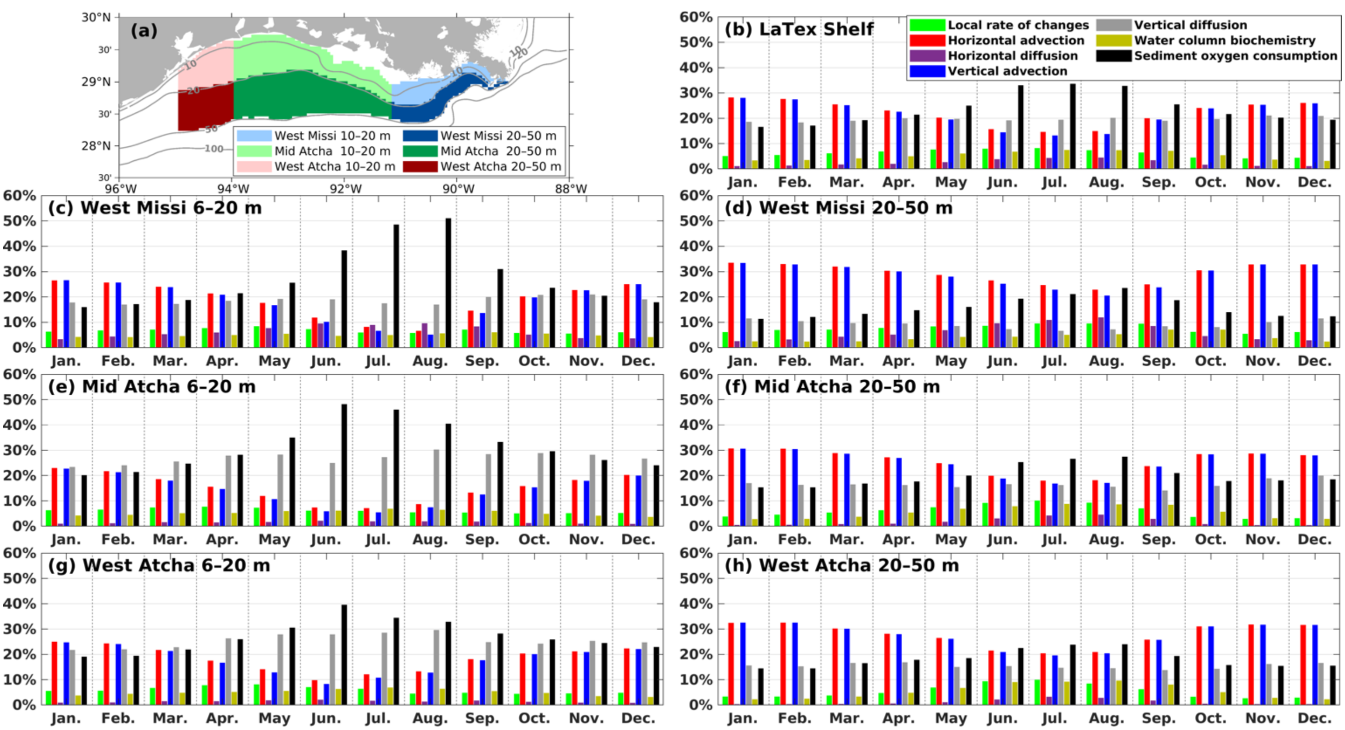

Figure 9. (a) Subregions defined by Fennel et al. (2016). Times series of monthly climatology (spatially averaged) of percentages of contribution (absolute values) from different hydrodynamic-related and biochemical-related terms over (b) the entire LaTex shelf, (c) west-Mississippi nearshore region (6–20 m), (d) west-Mississippi offshore region (20–50 m), (e) mid-Atchafalaya nearshore region, (f) mid-Atchafalaya offshore region, (g) west-Atchafalaya nearshore region, and (h) west-Atchafalaya offshore region.

4.2 Stratification and Bottom DO Advection/Diffusion

Sedimentary biochemical and hydrodynamics were found almost equally important in modulating the summer bottom DO in the nearshore regions (33%–51% vs 28%–55%). Nevertheless, in the offshore regions, contributions from hydrodynamics (51%–59%) outcompeted the impacts from SOC (19%–27%), which was consistent with the findings by Yu et al. (2015) and Mattern et al. (2013). Previous studies showed that water stratification regulated the oxygen replenishment and hypoxia dynamics in the LaTex shelf (Hetland and DiMarco, 2008; Bianchi et al., 2010; Fennel et al., 2011, 2013, 2016; Justić and Wang, 2014; Wang and Justić, 2009; Feng et al., 2014; Yu et al., 2015; Laurent et al., 2018). Water stratification can serve as an important index for the bottom DO advection and vertical diffusion processes and can be evaluated by the calculation of potential energy anomaly (PEA in J m^{-3}) :

$$PEA = \frac{1}{H}\int_{-h}^{\eta}(\bar{\rho} - \rho)gzdz, \qquad (12)$$

Where ρ is water density profile over water column of depth $H = h + \eta$, h is the location of the bed, η is water surface elevation, g is the gravitational acceleration (9.8 m s^{-2}), z is the vertical axis, $\bar{\rho}$ is the depth-integrated water density given by $\bar{\rho} = \frac{1}{H}\int_{-h}^{\eta}\rho dz$ (Simpson and Hunter, 1974; Simpson et al., 1978; Simpson, 1981; Simpson and Bowers, 1981). PEA represents the amount of energy per volume required to homogenize the entire water column. A greater PEA value represents a more stratified water column. We then compared the PEA with the absolute bottom DO advection and vertical diffusion of DO across the bottom layer. It was worth mentioning that the absolute bottom DO advection represents the exchanges of DO at the bottom layer due to advective processes, and that vertical diffusion of DO across the bottom layer was found almost positive in the 15-year simulations (99.99% of simulated records). In other words, the vertical diffusion replenished DO to the bottom layer most of the time on the shelf.

Significant negative linear correlations were found between the PEA and the two absolute advection terms of bottom DO (Fig. 10a and 10c; *r*=-0.73 between PEA and horizontal advection and *r*=-0.76 between PEA and vertical advection), indicating that the enhanced water stratification in summer usually leads to less DO exchanges duo to advection at the bottom layer. Scatter plots and the simple linear regression also showed a strong linear relationship between water stratification and absolute bottom DO advection. The impacts of biochemical processes on the bottom DO advection could not be neglected as biogeochemistry contributed directly to the local DO changes while DO advection was determined by both mean flow and spatial gradients of DO. This can also explain why the linear correlations between PEA and absolute bottom DO advection were not y close to -1. In contrast to the advection terms, bottom DO flux due to vertical diffusion was found positively and moderately correlated to the PEA (Fig. 10e, *r*=0.46). As the water column stability was enhanced in early summer, vertical diffusion of DO through the pycnocline would be suppressed (Bianchi et al., 2010; Rabalais and Turner, 2019), while in the lower water column, downward diffusion of DO to the bottom layer would be generally reinforced because of noticeable upward DO concentration gradients between the bottom and the above water layers. Such gradients resulted from the increasing SOC and decreasing DO exchanges by advection in early summer. However, as the strongly stratified water columns persisted, continuous DO removals due to SOC and decreasing DO supply from the upper layers drew down the DO level at both the bottom and the above layers. A lower vertical gradient of DO concentration and a weakened downward DO diffusion to the bottom layer was expected (e.g., summer in 2011, 2015, and 2019 in Fig. 10e). The scatter plot and the quadratic regression (Fig. 10f) highlighted such non-linear responses.

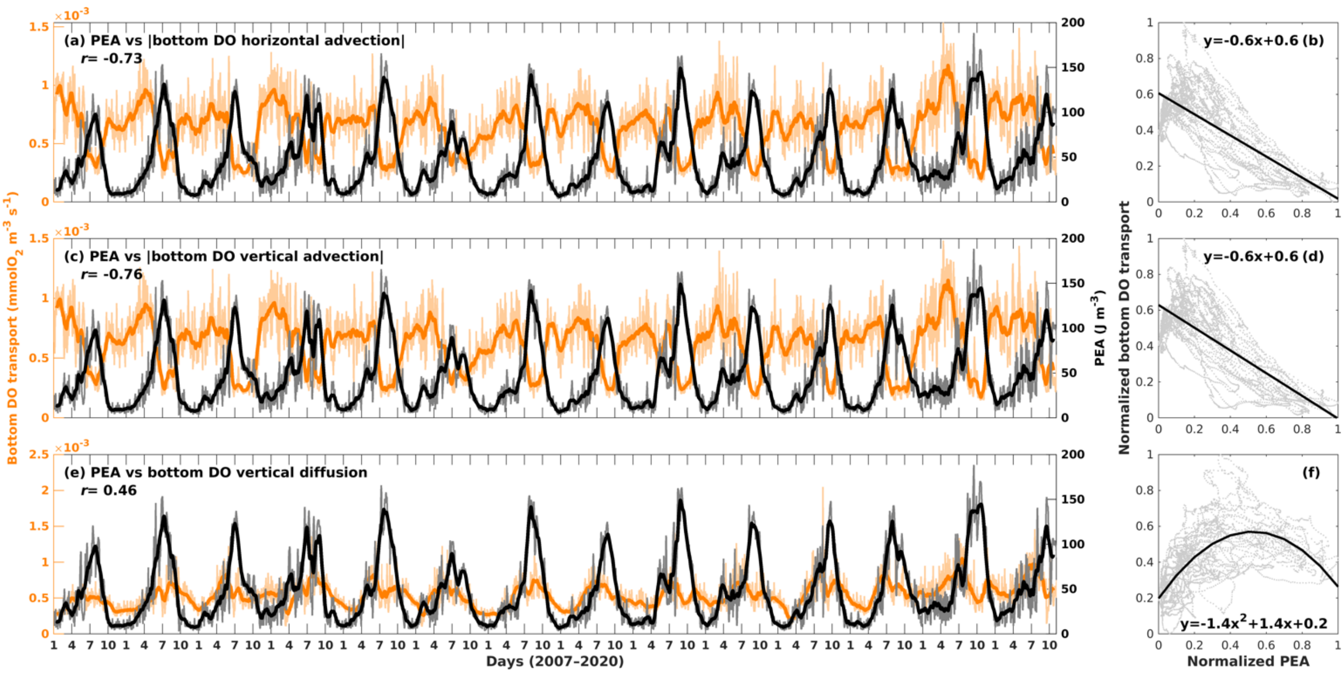

Figure 10. Comparison of daily time series (spatially averaged over the entire LaTex shelf, Fig. 2b) of PEA and the dominated bottom DO transport terms (i.e., (a) absolute horizontal advection, (c) absolute vertical advection, and € vertical diffusion. The symbol |.| represents the absolute operator. The light and bold lines shown represent original daily records and 31-day running smooth records, respectively. Linear correlations between the smooth records were also provided. Scatter plots and regression curves of the normalized smooth records (b) between PEA and absolute horizontal advection, (d) between PEA and absolute vertical advection, and (f) between PEA and vertical diffusion. The normalization method applied scales the records within a range from 0 to 1 according to the corresponding minimums and maximums.

4.3 Riverine nutrient reductions

Since 2001, the Mississippi River/Gulf of Mexico Hypoxia Task Force has set up a goal of controlling the size of mid-summer hypoxic zone below 5000 km^2 in a 5-year running average (Mississippi River/Gulf of Mexico Watershed Nutrient Task Force, 2001; 2008) by reducing riverine nutrient loads. Fennel and Laurent (2018) suggested that a reduction of 63 ± 18% (referred to as the 2000–2016 average) in total nitrogen loads or a dual reduction of 48 ± 21% in total nitrogen and phosphorus loads could be necessary to fulfill the hypoxia reduction goal. Statistic models (Scavia et al., 2013; Obenour et al., 2015; Turner et al., 2012; Laurent and Fennel, 2019) suggested a nutrient reduction of 52%–58% related to the 1980–1996 average would be enough to fulfill the goal. Nonetheless, inorganic nutrient types considered in these statistic models were nitrogen-based (i.e., ammonia and nitrite+nitrate) and phosphorus-based (i.e., phosphate) nutrients. The lower trophic community embedded in existing models was simplified with one phytoplankton functional group and one zooplankton functional group (e.g., Fennel et al., 2006, 2011, 2013; Fennel and Laurent, 2018; Justić and Wang, 2014). When applied to the LaTex shelf where diatom dominates the phytoplankton community, these models assume that the silicate supply in the shelf is excessive and the competition among different phytoplankton groups is not important to the DO variability. In this section, we aimed to explore the sensitivity of bottom DO to the riverine nutrient discharge with different combinations, the corresponding changes in plankton biomass, the complexity of the lower trophic community, and its implication for hypoxia reduction.

Table 3. Riverine inorganic nutrient reduction percentages for different sensitivity experiments. Note that all the runs listed were initialized on 1 August 2017 and were conducted from 1 August 2017 to 26 August 2020.

	Riverine inorganic nutrients reduction percentages (%)		
	N	P	Si
EXPcontrol	0	0	0
EXPN20	20	0	0
EXPN40	40	0	0
EXPN60	60	0	0
EXPN80	80	0	0
EXPP20	0	20	0
EXPP40	0	40	0
EXPP60	0	60	0
EXPP80	0	80	0
EXPSi20	0	0	20
EXPSi40	0	0	40
EXPSi60	0	0	60
EXPSi80	0	0	80
EXPNPSi20	20	20	20
EXPNPSi40	40	40	40
EXPNPSi60	60	60	60
EXPNPSi80	80	80	80

A total of 16 sensitivity experiments were set up with different combinations of the riverine inorganic nutrient concentration and river freshwater discharges remained the same as in the control run. To remove numerical bias introduced by initial conditions and to reduce computational efforts, both control run and sensitivity experiments were initialized on 1 August 2017 and were conducted from 1 August 2017 to 26 August 2020. Initial conditions were derived from the 15-year hindcast. Analysis and comparisons were conducted based on simulations from 1 January 2018 to 26 August 2020. In summer, SOC is the prevailing factor in bottom DO changes (Fig. 9) over the shelf. When the hydrodynamics remain the same, changes in the size of hypoxia water are a result of the changes in the riverine nutrient inputs. The hypoxia averaged through the 2018–2020 summer shelf-wide cruises from the control run, and sensitivity experiments were shown in Fig. 11. To illustrate the complexity of the lower trophic community regarding decreased nutrient loads as well their contribution to the hypoxia development, simulated plankton (i.e., PS, PL, ZS, ZL, and ZP) concentration of the sensitivity experiments was also shown.

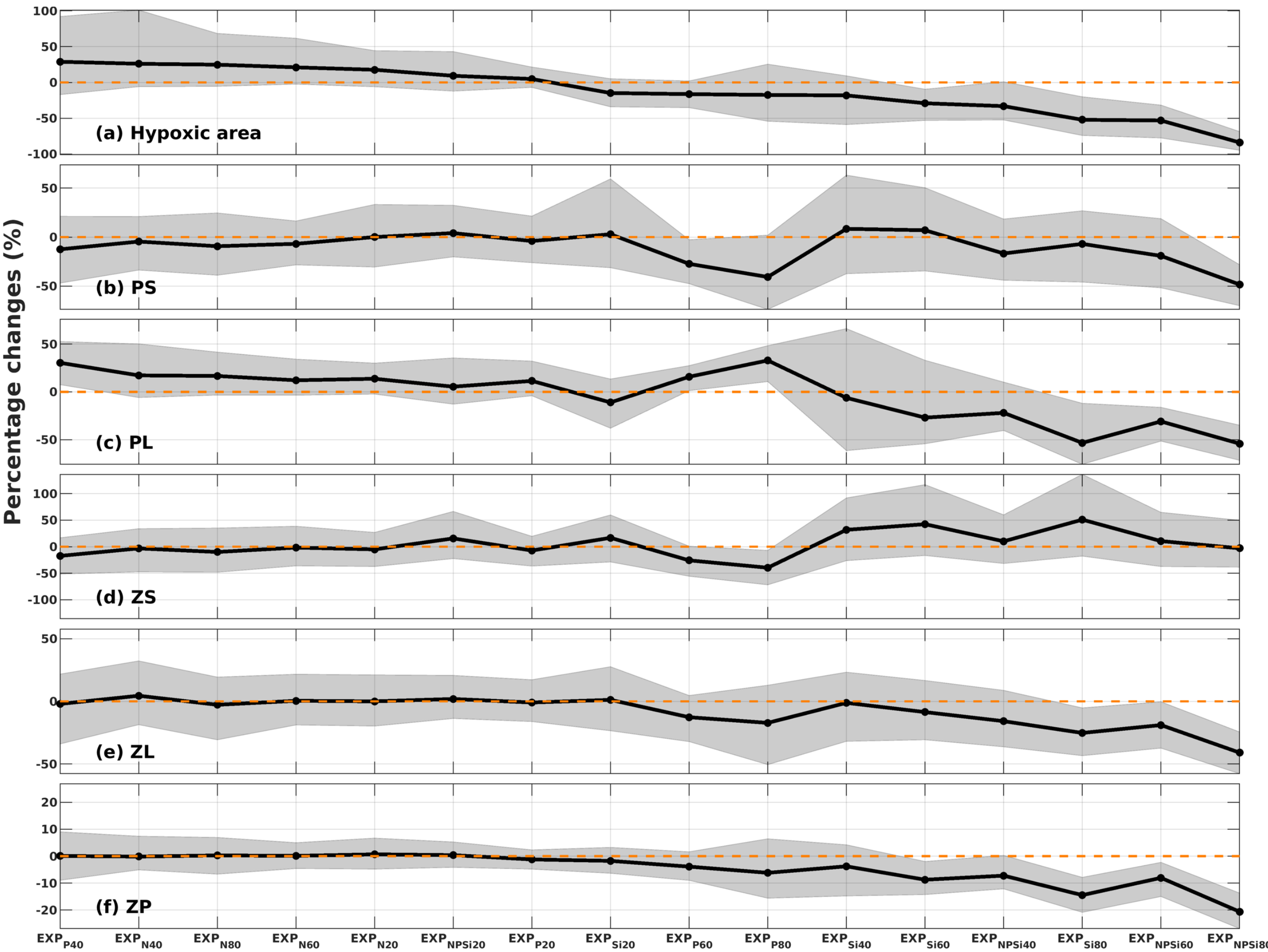

Figure 11. Percentage differences of multi-yearly summer mean (spatially averaged over the LaTex shelf of 6–50 m) of (a) hypoxic area during the shelf-wide cruises, (b) PS, (c) PL, (d) ZS, (e) ZL, and (f) ZP between the 16 sensitivity runs and the control run. The solid black curves indicate the multi-yearly summer means, while the grey region denotes the ranges of the 10–90 percentiles. The dashed orange lines indicate the 0% of changes. Note that the statistics shown are sorted according to the mean percentage changes in the hypoxic area.

As a more complex plankton community was embedded than in previous modeling studies, we found that a sole nutrient reduction in nitrogen would not guarantee decreases in the hypoxic area (Fig. 11a); on the contrary, it would generally lead to an increase in the hypoxic zone. The averaged PS concentration would decrease by ~5% due to the reduced nitrogen supply. However, the average PL concentration would increase by ~15%. Zooplankton concentration would not change much. It could also be seen in the spatial patterns of concentration differences (e.g., EXP_{N80}, Fig. 12). The decrease (increase) in bottom DO over the west (east) shelf would be consistent with the increasing (decreasing) PL concentration. The competition between different phytoplankton groups would lead to different responses of phytoplankton concentration to the changing nutrient environments. In the meantime, the responses of the secondary production to the changing nutrient supply could be less straightforward than the primary production due to the complex energy flows associated with grazing and predation processes. Thus, it is necessary to consider the complexity of the lower-trophic community as an important proxy for the impacts of nutrient reduction strategies on shelf hypoxia.

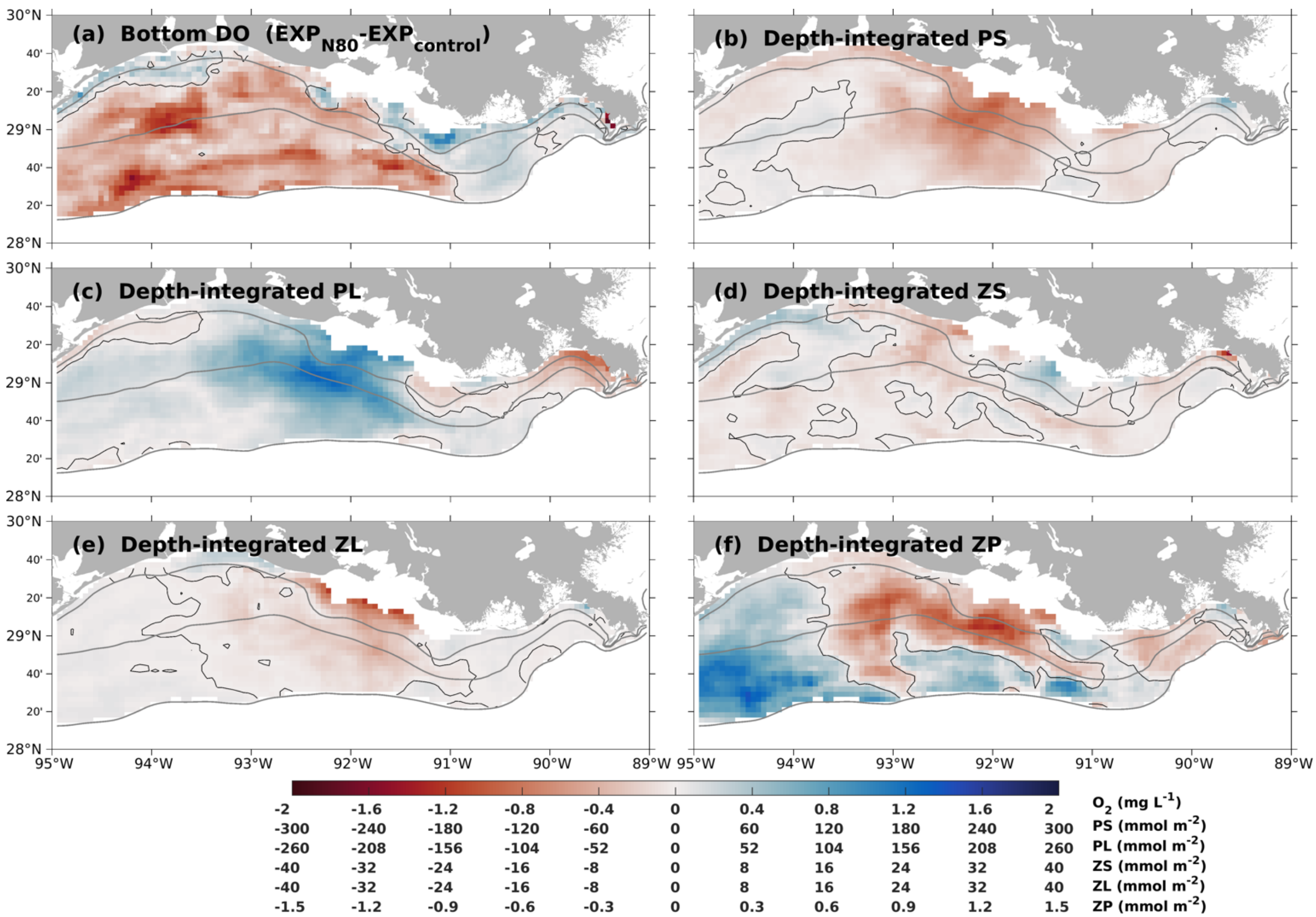

Figure 12. Multi-yearly (2018–2020) summer (period covered by mid-summer shelf-wide cruise) mean of model simulations differences between EXP_{N80} and $EXP_{control}$ for (a) bottom DO concentration (mg L^{-1}) and depth-integrated concentration (mmol m^{-2}) of different plankton groups (i.e., (b) PS, (c) PL, (d) ZS, (e) ZL, and (f) ZP).

Sensitivity studies on phosphorus reduction also highlighted the importance of plankton competition in hypoxic area distribution. A sole 60% reduction of phosphorus could reduce the shelf hypoxic area by ~16% (Fig. 11). Such a change could be attributed to a remarkable shrinkage of the PS community and the resulting decreases in secondary productivity (e.g., EXP_{P80};

Fig. 13b, 13d–13f). This result is consistent with that in Laurent and Fennel (2014), which indicates a decrease of 13% in the hypoxic area when the riverine phosphorus supply is halved. Nevertheless, the correlation between phosphorus cut and reduction of hypoxia area was found not linear- the hypoxic zone was expected to increase with a low (EXP_{P20}) or moderate (EXP_{P40}) reduction in phosphorus, mainly owing to the competition between PS and PL (Fig 11). One should also note that the DO over the shelf would not evenly respond to the reduced phosphorus loads. The bottom DO could decrease on the west shelf (nearshore; Fig. 13a) in response to an 80% phosphorus cut because the increases in PL concentration could exceed the decreases in other plankton biomass.

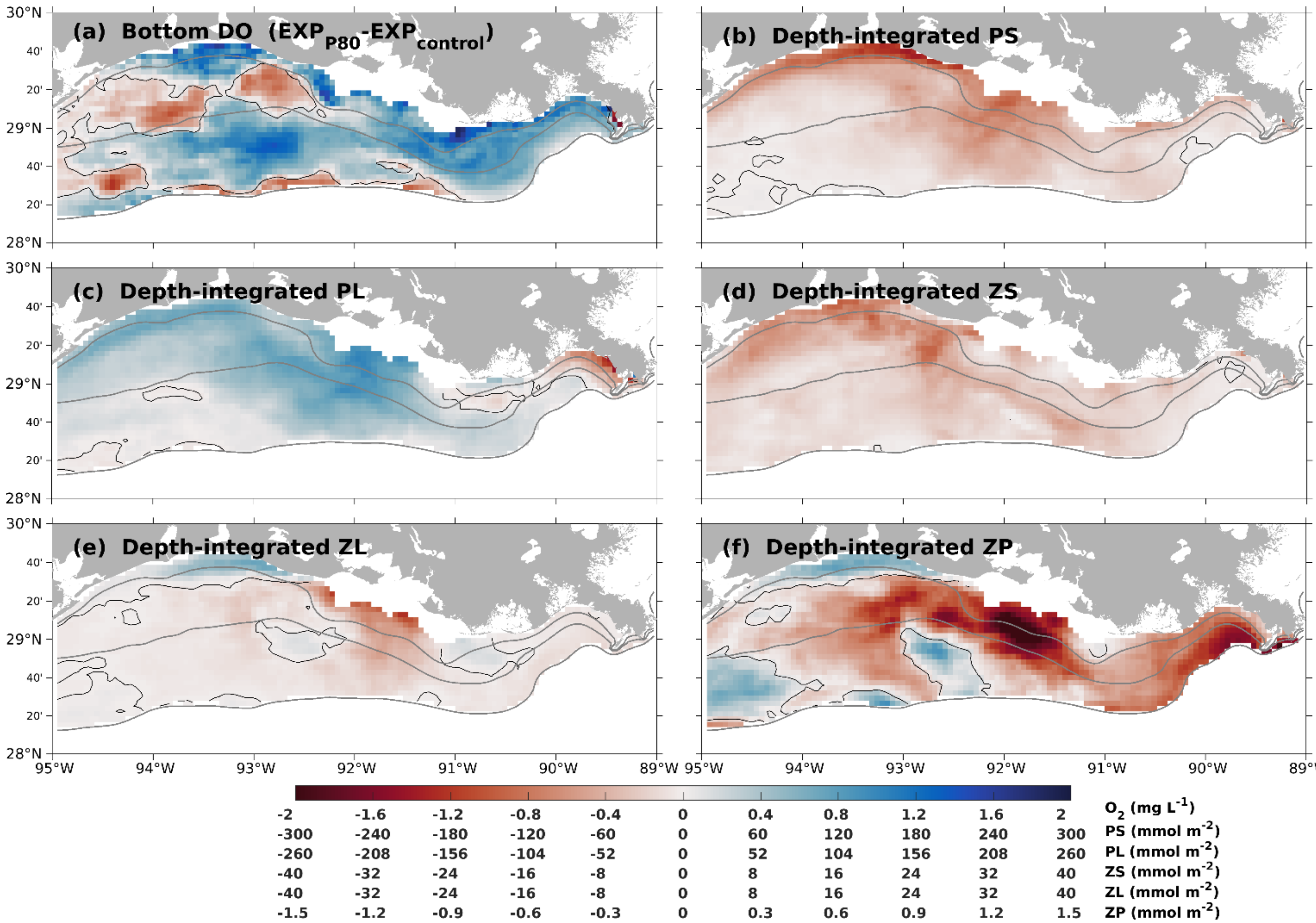

Figure 13. Same as Figure 12, but between EXP_{P80} and $EXP_{control}$.

The hypoxic area would exhibit an acute reduction when riverine silicon supply was limited (Fig. 11), which was attributed to the corresponding declines in PL and resulting ZL and ZP concentrations (Fig. 11 and Fig. 14). When riverine silicon supply was reduced by 80%, the hypoxic area would be expected to decrease by 50% (to 8126 km^2). Compared with the control run, the bottom DO of EXP_{Si80} would exhibit an overall increase corresponding to the PL (diatom) reduction. As diatom is the dominant phytoplankton group in the LaTex shelf, there is no surprise that a remarkable decrease in PL would lead to a pronounced reduction in hypoxic area and an increase in bottom DO. Nevertheless, elevated DO was not simulated all over the shelf. For example, we found DO would be decreased near the Mississippi River mouth, where PL was reduced while other plankton groups were increased.

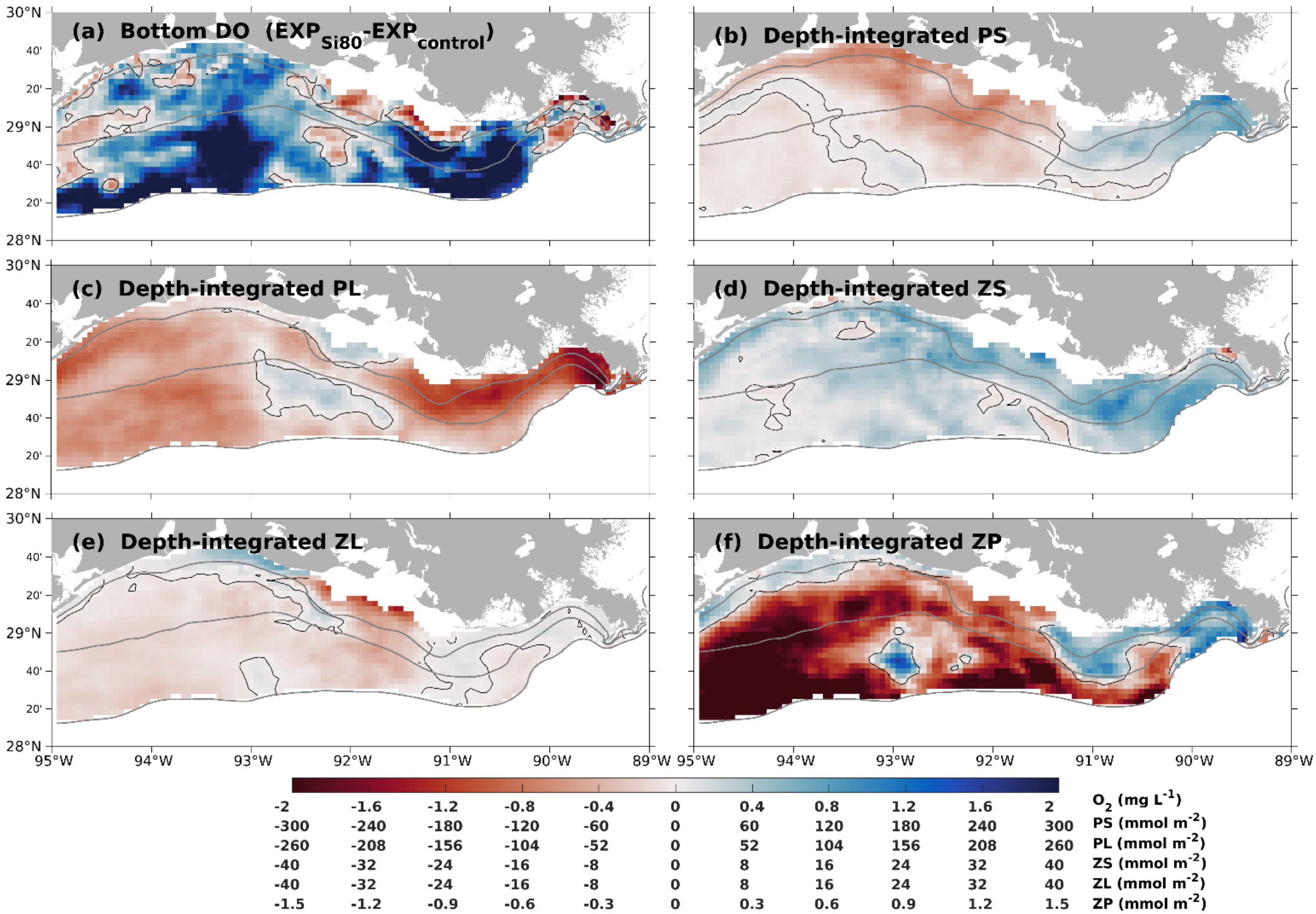

Figure 14. Same as Figure 12, but between EXP_{Si80} and $EXP_{control}$.

The PS and PL could perform differently in response to the nutrient reductions. Unlike a sole reduction of silicon, sole reductions of nitrogen or phosphorus loads tended to suppress PS growth but in contrast, lead to an increase in PL concentration due to less competition (Fig. 11–14). Such different responses in the primary production would induce different changes in the secondary productions and together would lead to uncertainties in the directions of SOC changes and thus the size of the hypoxic area. So far model simulations showed that a sole silicon reduction could be the best for reducing hypoxia. We further tested the sensitivity of hypoxic area changes to triple reduction strategies. The 3-year mean hypoxic area would decrease by

53% (to 8223 km^2) and 84% (to 2999 km^2) when all nutrient supplies were reduced simultaneously by 60% and 80%, respectively (Fig. 11). Thus, it is expected that the 3-year mean hypoxic area can reach the hypoxia goal of 5000 km^2 if all nutrients are reduced by nearly 80%. The spatial distribution of the differences between EXP_{NPSi80} and the control run suggested a massive and sharp increase in bottom DO over the shelf attributed to the massive decrease in both primary and secondary productions (Fig. 15). One should also note that similar to the sole reduction cases, a reduction in all three nutrient loads could also result in an increase in hypoxic area (e.g., the hypoxic area increased by 9% in EXP_{NPSi20}; Fig. 11) due to the competition among different plankton groups. Uncertainties introduced by lower-trophic community complexity are responsible for such nonlinear responses of biomass and bottom DO to nutrient reductions. To meet the hypoxia goal, the recommended percentage on nutrient loads reduction indicated by previous model studies tended to be less than the suggested percentage by our simulations (~80%). In addition, a complex plankton community enables a longer resident time or more efficient recycling of nutrients in the system than the simple models. These results shed lights on the needs of a comprehensive evaluation of DO's response regarding the proposed Hypoxia Task Force nutrient reduction plan.

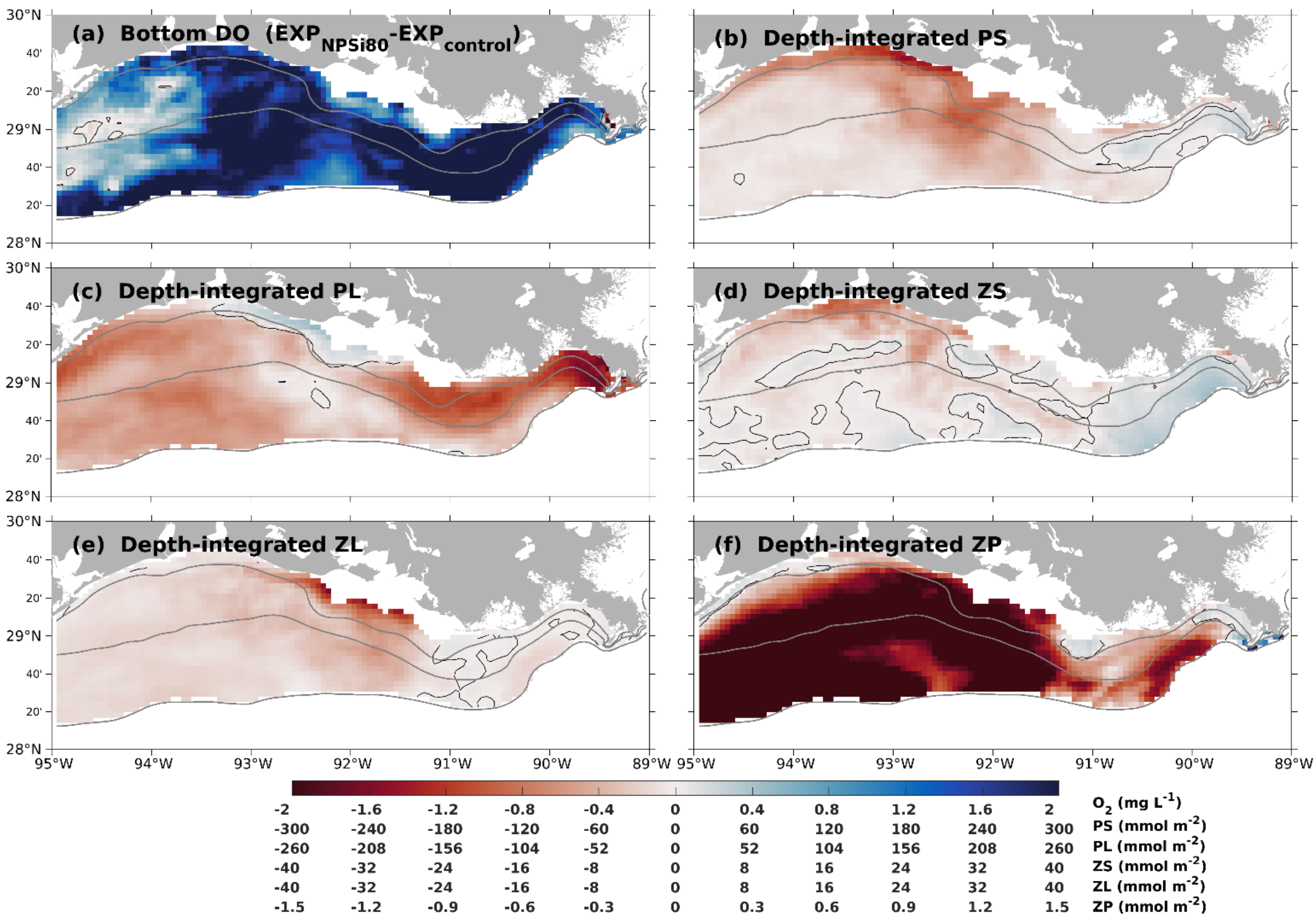

Figure 15. Same as Figure 12, but between EXP_{NPSi80} and $EXP_{control}$.

5 Conclusions

A three-dimensional coupled hydrodynamic–biogeochemical model (NEMURO) was modified and applied to the Gulf of Mexico to study the bottom DO variability in the LaTex Shelf. In addition to nitrogen and silicon, a phosphorous flow was embedded into the NEMURO model to account for the impacts of phosphorous limitation on hypoxia development. Built on the SOC scheme of the instantaneous remineralization developed by Fennel et al. (2006), a pool of sedimentary PON was added to account for temporal delays in SOC to the peak of plankton blooms. The model can well reproduce the vertical profiles of inorganic nutrient concentration (i.e., nitrate, phosphate, and silicate), the ratio of diatom/total phytoplankton, SOC, and the ratio of SOC/overlaying water respiration. The model's robustness in DO simulation was affirmed via 1) comparison of the DO profiles against cruise observations from three different databases, 2) comparison of spatial distributions of bottom DO, and 3) time series of the hypoxic area against the shelf-wide cruises observations.

A 15-year coupled physical-biogeochemical hindcast was achieved covering the period of 2006-2020. Three DO transport terms (i.e., horizontal advection, vertical advection, and vertical diffusion) and a biochemical term (i.e., SOC) were found as the most influential factors modulating the bottom DO dynamics in the LaTex shelf. They jointly contributed ~80% of the variability in bottom DO throughout the year. Specifically, the contribution of SOC (34%) outcompetes other factors in summer. In different subregions of the shelf, the contributions of the four terms vary with depth and distance from the Mississippi River mouth. In the nearshore regions, SOC plays a much more important role in modulating the summer bottom DO concentration with a maximum contribution of 33%–51%; while in the offshore regions, its contribution decreases notably to 19%–27% in summer, which is comparable to the contributions of the other three hydrodynamic-induced terms (18%–26% for the horizontal advection, 17%–25% for the vertical advection, and 7%–16% for the vertical diffusion).

If the advection and vertical diffusion are considered jointly as a hydrodynamic term, the impacts of SOC (33%–51%) and hydrodynamics (28%–55%) are almost equally important in modulating the summer bottom DO in the nearshore regions, while in the offshore areas, contributions from hydrodynamics (51%–59%) outcompete the SOC impacts (19%–27%). The strong linear correlations between PEA and the advection terms suggest that increased water stability in summer leads to weaker DO exchanges from advection processes. Nevertheless, the relationship between PEA and vertical diffusion of DO across the bottom layer appears to be non-linear. As PEA starts to increase in early summer, the bottom DO starts to drop, resulting in strong vertical DO gradients at the bottom layer and enhanced vertical diffusion. As the strong water column stratification persists in mid and late summer, vertical diffusion of DO tends to be suppressed due to the weaker DO gradient resulting from the continuous DO consumption and the decreasing DO supply from the upper layers.

We further examined the sensitivity of summer bottom DO to riverine nutrient reductions. Our sensitivity experiments highlighted the importance of the complexity of the lower-trophic community in bottom DO's response to the changing nutrient loads. Sole nutrient reductions in total nitrogen do not guarantee a hypoxic area decrease. Reduced nitrogen load can stimulate the competition between PS and PL and uncertainties to secondary productivity. Sole phosphorous reductions can, in general, reduce hypoxic area as PS and associated decreases in secondary productivity are reduced. A silicon reduction is more effective in reducing the hypoxic zone than the other two nutrients exhibited by the reductions in PL, ZS, and ZP concentration. One should also note that changes in the bottom DO are not evenly distributed over the shelf. A triple reduction strategy for all nutrients performs the best in reducing shelf hypoxic areas. When riverine nitrogen, phosphorous, and silicon loads are reduced by ~80% simultaneously, the hypoxia reduction goal of 5000 km^2 is likely to be achieved.

Code/Data availability: Model data is available at the LSU mass storage system and details are on the webpage of the Coupled Ocean Modeling Group at LSU (https://faculty.lsu.edu/zxue/). Data requests can be sent to the corresponding author via this webpage.

Author contribution: Z. George Xue designed the experiments and Yanda Ou carried them out. Yanda Ou developed the model code and performed the simulations. Yanda Ou and Z. George Xue prepared the manuscript.

Competing interests: The authors declare that they have no conflict of interest.

Acknowledgment: Research support was provided through the Bureau of Ocean Energy Management (M17AC00019, M20AC10001). We thank Dr. Jerome Fiechter at UC Santa Cruz for sharing his NEMURO model codes and Dr. Katja Fennel at Dalhouse University for discussing model parameterization. The computational resource was provided by the High-Performance Computing Facility (clusters SuperMIC and QueenBee3) at Louisiana State University.

Appendix A: Expressions of processes terms modified in this study

Detailed descriptions of related terms and parameters are listed in Appendix B.

A1 Update gross primary production of PS and PL due to the additional phosphate limitation

$$GppPSn = GppNPS + GppAPS, \quad \text{(A1)}$$

$$GppPLn = GppNPL + GppAPL, \quad \text{(A2)}$$

where,

$$GppNPS = PSn\, V_{maxS}\, exp\left(K_{GppS}\, TMP\right)\left[1 - exp\left(-\frac{\alpha_{PS}}{V_{maxS}} I_{PS}\right)\right] exp\,(-\frac{\beta_{PS}}{V_{maxS}} I_{PS})\; NutlimPS\; RnewS, \quad \text{(A3)}$$

$$GppAPS = PSn\, V_{maxS}\, exp\left(K_{GppS}\, TMP\right)\left[1 - exp\left(-\frac{\alpha_{PS}}{V_{maxS}} I_{PS}\right)\right] exp\,(-\frac{\beta_{PS}}{V_{maxS}} I_{PS})\; NutlimPS\; (1 - RnewS), \quad \text{(A4)}$$

$$GppNPL = PLn\, V_{maxL}\, exp\left(K_{GppL}\, TMP\right)\left[1 - exp\left(-\frac{\alpha_{PL}}{V_{maxL}} I_{PL}\right)\right] exp\left(-\frac{\beta_{PL}}{V_{maxL}} I_{PL}\right) NutlimPL\; RnewL, \quad \text{(A5)}$$

$$GppAPL = PLn\, V_{maxL}\, exp\left(K_{GppL}\, TMP\right)\left[1 - exp\left(-\frac{\alpha_{PL}}{V_{maxL}} I_{PL}\right)\right] exp\left(-\frac{\beta_{PL}}{V_{maxL}} I_{PL}\right) NutlimPL\; (1 - RnewL), \quad \text{(A6)}$$

$$RnewS = \frac{NO_3}{(NO_3 + K_{NO_3S})\left(1 + \frac{NH_4}{K_{NH_4S}}\right)} \frac{1}{\frac{NO_3}{(NO_3 + K_{NO_3S})\left(1 + \frac{NH_4}{K_{NH_4S}}\right)} + \frac{NH_4}{NH_4 + K_{NH_4S}}}, \quad \text{(A7)}$$

$$RnewL = \frac{NO_3}{(NO_3 + K_{NO_3L})\left(1 + \frac{NH_4}{K_{NH_4L}}\right)} \frac{1}{\frac{NO_3}{(NO_3 + K_{NO_3L})\left(1 + \frac{NH_4}{K_{NH_4L}}\right)} + \frac{NH_4}{NH_4 + K_{NH_4L}}}, \quad \text{(A8)}$$

$$NutlimPS = min\left(\frac{NO_3}{(NO_3 + K_{NO_3S})\left(1 + \frac{NH_4}{K_{NH_4S}}\right)} + \frac{NH_4}{NH_4 + K_{NH_4S}}, \frac{PO_4}{PO_4 + K_{PO_4S}}\right), \quad \text{(A9)}$$

$$NutlimPL = min\left(\frac{NO_3}{(NO_3 + K_{NO_3L})\left(1 + \frac{NH_4}{K_{NH_4L}}\right)} + \frac{NH_4}{NH_4 + K_{NH_4L}}, \frac{PO_4}{PO_4 + K_{PO_4L}}, \frac{SiOH_4}{SiOH_4 + K_{SiOH_4L}}\right), \quad \text{(A10)}$$

$$I_{PS} = PAR\; frac\; exp\left\{z\; AttSW + AttPS \int_z^0 [PSn(\zeta) + PLn(\zeta)]\, d\zeta\right\}, \quad \text{(A11)}$$

$$I_{PL} = PAR\; frac\; exp\left\{z\; AttSW + AttPL \int_z^0 [PSn(\zeta) + PLn(\zeta)]\, d\zeta\right\}, \quad \text{(A12)}$$

A2 Update aerobic decomposition from PON to NH_4 and from DON to NH_4 due to introduction of oxygen dependency

$$DecP2N = PON\; VP2N_0\; exp(K_{P2N}\, TMP)\, \hat{r}, \quad \text{(A13)}$$

$$DecD2N = PON\; VD2N_0\; exp(K_{D2N}\, TMP)\, \hat{r}, \quad \text{(A14)}$$

where,

$$\hat{r} = max\left[\frac{max(0, Oxyg - Oxyg_{th})}{K_{Oxyg} + Oxyg - Oxyg_{th}}, 0\right], \quad \text{(A15)}$$

A3 Update water column nitrification due to introduction of oxygen dependency and light limitation

$$Nit = Nit_0 exp(K_{Nit}\ TMP)\ LgtlimN\ \hat{r}, \quad \text{(A16)}$$

where,

$$LgtlimN = 1 - max\left(0, \frac{I_N - I_0}{I_N - I_0 + k_I}\right), \quad \text{(A17)}$$

$$I_N = PAR\ frac\ exp\left\{z\ AttSW + max(AttPS, AttPL) \int_z^0 [PSn(\zeta) + PLn(\zeta)] d\zeta\right\}, \quad \text{(A18)}$$

A4 Additional SOC term:

$$SOC = 8.3865\ PON_{sed}\ VP2N_0\ \ exp(K_{P2N}\ TMP), \quad \text{(A19)}$$

Appendix B: Descriptions of terms and parameters

Table B1. Descriptions of state variables

Terms	Description	Unit
NH_4	Ammonium concentration	mmolN m^{-3}
NO_3	Nitrate concentration	mmolN m^{-3}
PO_4	Phosphate concentration	mmolP m^{-3}
DOP	Dissolved organic phosphorous concentration	mmolP m^{-3}
POP	Particulate organic phosphorous concentration	mmolP m^{-3}
$SiOH_4$	Silicate concentration	mmolSi m^{-3}
PSn	Small phytoplankton biomass concentration measured in nitrogen	mmolN m^{-3}
PLn	Large phytoplankton biomass concentration measured in nitrogen	mmolN m^{-3}
$Oxyg$	Dissolved oxygen concentration	mmolO_2 m^{-3}

Table B2 Descriptions of related terms involved in the phosphorus cycle and nutrient limitation. Superscripts "*" and "+" denote that the mathematic expressions of corresponding terms are the same as those in Kishi et al. (2007) and Shropshire et al. (2020), respectively. Expressions of terms with no superscript are updated and reported in Appendix A.

Terms	Description	Unit
$DecP2N$	Decomposition rate from PON to NH_4	mmolN m^{-3} day^{-1}
$DecD2N$	Decomposition rate from DON to NH_4	mmolN m^{-3} day^{-1}
$DecP2D^{*+}$	Decomposition rate from PON to DON	mmolN m^{-3} day^{-1}
$EgeZLn^{+}$	Large zooplankton egestion rate measured in nitrogen	mmolN m^{-3} day^{-1}
$EgeZPn^{*+}$	Predatory zooplankton egestion rate measured in nitrogen	mmolN m^{-3} day^{-1}

$EgeZSn^{*+}$	Small zooplankton egestion rate measured in nitrogen	mmolN m^{-3} day^{-1}
$ExcPSn^{*+}$	Small phytoplankton extracellular excretion rate to DON and is measured in nitrogen	mmolN m^{-3} day^{-1}
$ExcPLn^{*+}$	Large phytoplankton extracellular excretion rate to DON and is measured in nitrogen	mmolN m^{-3} day^{-1}
$ExcZSn^{*+}$	Small zooplankton excretion rate to NH_4 and is measured in nitrogen	mmolN m^{-3} day^{-1}
$ExcZLn^{+}$	Large zooplankton excretion rate to NH_4 and is measured in nitrogen	mmolN m^{-3} day^{-1}
$ExcZPn^{*+}$	Predatory zooplankton excretion rate to NH_4 and is measured in nitrogen	mmolN m^{-3} day^{-1}
$GppNPS$	Small phytoplankton nitrate-induced gross primary production rate measured in nitrogen	mmolN m^{-3} day^{-1}
$GppAPS$	Small phytoplankton ammonium-induced gross primary production rate measured in nitrogen	mmolN m^{-3} day^{-1}
$GppPSn$	Small phytoplankton gross primary production rate measured in nitrogen	mmolN m^{-3} day^{-1}
$GppNPL$	Large phytoplankton nitrate-induced gross primary production rate measured in nitrogen	mmolN m^{-3} day^{-1}
$GppAPL$	Large phytoplankton ammonium-induced gross primary production rate measured in nitrogen	mmolN m^{-3} day^{-1}
$GppPLn$	Large phytoplankton gross primary production rate measured in nitrogen	mmolN m^{-3} day^{-1}
$MorPSn^{+}$	Small phytoplankton mortality rate measured in nitrogen	mmolN m^{-3} day^{-1}
$MorPLn^{+}$	Large phytoplankton mortality rate measured in nitrogen	mmolN m^{-3} day^{-1}
$MorZSn^{+}$	Small zooplankton mortality rate measured in nitrogen	mmolN m^{-3} day^{-1}
$MorZLn^{+}$	Large zooplankton mortality rate measured in nitrogen	mmolN m^{-3} day^{-1}
$MorZPn^{*+}$	Predatory zooplankton mortality rate measured in nitrogen	mmolN m^{-3} day^{-1}
Nit	Nitrification rate	mmolN m^{-3} day^{-1}
$ResPSn^{*+}$	Small phytoplankton respiration rate measured in nitrogen	mmolN m^{-3} day^{-1}
$ResPLn^{*+}$	Large phytoplankton respiration rate measured in nitrogen	mmolN m^{-3} day^{-1}
SOC	Sediment oxygen consumption rate	mmolO_2 m^{-2} day^{-1}

Table B3 Descriptions of other variables

Terms	Description	Unit
I_{PS}	Photosynthetically available radiation for small phytoplankton	W m^{-2}
I_{PL}	Photosynthetically available radiation for large phytoplankton	W m^{-2}
I_N	Maximum photosynthetically available radiation	W m^{-2}
$LgtlimN$	Light inhibition on nitrification rate	no dimension
$NutlimPS$	Nutrient limitation term for small phytoplankton	no dimension
$NutlimPL$	Nutrient limitation term for large phytoplankton	no dimension
PAR	Net short-wave radiation on water surface	W m^{-2}
$\hat{r}$	Oxygen inhibition on nitrification and aerobic decomposition rates	no dimension
$RnewS$	The f-ratio of small phytoplankton which is defined by the ratio of nitrate uptake to total uptake of nitrate and ammonium	no dimension
$RnewL$	The f-ratio of large phytoplankton which is defined by the ratio of nitrate uptake to total uptake of nitrate and ammonium	no dimension
$Thickness_{bot}$	Thickness of the bottom water layer	m
TMP	Water temperature	°C
z, ζ	Vertical coordinate which is negative below sea surface	m

Table B4. Descriptions and values of all model parameters. Superscripts "S", "L", "F06", and "F13" denote that the corresponding parameters follow Shropshire et al. (2020), Laurent et al. (2012), Fennel et al. (2006), and Fennel et al. (2013), respectively. Superscript "*" indicates the corresponding parameters are from this study.

Parameter	Description	Units	Values
	Small phytoplankton		
V_{maxS}	Small phytoplankton maximum photosynthetic rate at 0 ℃	day^{-1}	0.4^{S}
K_{NO_3S}	Small Phytoplankton half saturation constant for nitrate	mmolN m^{-3}	0.5^{S}
K_{NH_4S}	Small Phytoplankton half saturation constant for ammonium	mmolN m^{-3}	0.1^{S}
K_{PO_4S}	Small Phytoplankton half saturation constant for phosphate	mmolP m^{-3}	0.5^{L}
α_{PS}	Small phytoplankton photochemical reaction coefficient, initial slope of P-I curve	m^{2} W^{-1} day^{-1}	0.1^{S}

β_{PS}	Small phytoplankton photoinhibition coefficient	$m^2\ W^{-1}\ day^{-1}$	0.00045^S
Res_{PS0}	Small phytoplankton respiration rate at 0 ℃	day^{-1}	0.03^S
Mor_{PS0}	Small phytoplankton mortality rate at 0 ℃	$m^3\ mmolN^{-1}\ day^{-1}$	0.002^S
γ_S	Ratio of extracellular excretion to photosynthesis for small phytoplankton	no dimension	0.135^S
K_{GppS}	Small phytoplankton temperature coefficient for photosynthetic rate	$℃^{-1}$	0.0693^S
K_{ResPS}	Small phytoplankton temperature coefficient for respiration	$℃^{-1}$	0.0519^S
K_{MorPS}	Small phytoplankton temperature coefficient for mortality	$℃^{-1}$	0.0693^S
	Large phytoplankton		
V_{maxL}	Large phytoplankton maximum photosynthetic rate at 0 ℃	day^{-1}	0.8^S
K_{NO_3L}	Large Phytoplankton half saturation constant for nitrate	$mmolN\ m^{-3}$	3.0^S
K_{NH_4L}	Large Phytoplankton half saturation constant for ammonium	$mmolN\ m^{-3}$	0.3^S
K_{PO_4L}	Large Phytoplankton half saturation constant for phosphate	$mmolP\ m^{-3}$	0.5^L
K_{SiOH_4L}	Large Phytoplankton half saturation constant for silicate	$mmolSi\ m^{-3}$	6.0^S
α_{PL}	Large phytoplankton photochemical reaction coefficient, initial slope of P-I curve	$m^2\ W^{-1}\ day^{-1}$	0.1^S
β_{PL}	Large phytoplankton photoinhibition coefficient	$m^2\ W^{-1}\ day^{-1}$	0.00045^S
Res_{PL0}	Large phytoplankton respiration rate at 0 ℃	day^{-1}	0.03^S
Mor_{PL0}	Large phytoplankton mortality rate at 0 ℃	$m^3\ mmolN^{-1}\ day^{-1}$	0.001^S

γ_L	Ratio of extracellular excretion to photosynthesis for large phytoplankton	no dimension	0.135^S
K_{GppL}	Large phytoplankton temperature coefficient for photosynthetic rate	$℃^{-1}$	0.0693^S
K_{MorPL}	Large phytoplankton temperature coefficient for mortality	$℃^{-1}$	0.0693^S
K_{ResPL}	Large phytoplankton temperature coefficient for respiration	$℃^{-1}$	0.0693^S
	Small zooplankton		
GR_{maxSps}	Small zooplankton maximum grazing rate on small phytoplankton at 0 ℃	day^{-1}	0.6^S
λ_S	Ivlev constant of small zooplankton	m^3 mmolN^{-1}	1.4^S
$PS2ZS$	Small zooplankton threshold value for grazing on small phytoplankton	mmolN m^{-3}	0.043^S
α_{ZS}	Assimilation efficiency of small zooplankton	no dimension	0.7^S
β_{ZS}	Growth efficiency of small zooplankton	no dimension	0.3^S
Mor_{ZS0}	Small zooplankton mortality rate at 0 ℃	m^3 mmolN^{-1} day^{-1}	0.022^S
K_{GraS}	Small zooplankton temperature coefficient for grazing	$℃^{-1}$	0.0693^S
K_{MorZS}	Small zooplankton temperature coefficient for mortality	$℃^{-1}$	0.0693^S
	Large zooplankton		
GR_{maxLps}	Large zooplankton maximum grazing rate on small phytoplankton at 0 ℃	day^{-1}	0^S
GR_{maxLpl}	Large zooplankton maximum grazing rate on large phytoplankton at 0 ℃	day^{-1}	0.3^S
GR_{maxLzs}	Large zooplankton maximum grazing rate on small zooplankton at 0 ℃	day^{-1}	0.3^S
λ_L	Ivlev constant of large zooplankton	m^3 mmolN^{-1}	1.4^S
$PL2ZL$	Large zooplankton threshold value for grazing on large phytoplankton	mmolN m^{-3}	0.040^S

$ZS2ZL$	Large zooplankton threshold value for grazing on small zooplankton	mmolN m^{-3}	0.040^{S}
α_{ZL}	Assimilation efficiency of large zooplankton	no dimension	0.7^{S}
β_{ZL}	Growth efficiency of large zooplankton	no dimension	0.3^{S}
Mor_{ZL0}	Large zooplankton mortality rate at 0 ℃	m^{3} mmolN^{-1} day^{-1}	0.022^{S}
K_{GraL}	Large zooplankton temperature coefficient for grazing	℃$^{-1}$	0.0693^{S}
K_{MorZL}	Large zooplankton temperature coefficient for mortality	℃$^{-1}$	0.0693^{S}
	Predatory zooplankton		
GR_{maxPpl}	Predatory zooplankton maximum grazing rate on large phytoplankton at 0 ℃	day^{-1}	0.1^{S}
GR_{maxPzs}	Predatory zooplankton maximum grazing rate on small zooplankton at 0 ℃	day^{-1}	0.1^{S}
GR_{maxPzl}	Predatory zooplankton maximum grazing rate on large zooplankton at 0 ℃	day^{-1}	0.3^{S}
λ_{P}	Ivlev constant of predatory zooplankton	m^{3} mmolN^{-1}	1.4^{S}
$PL2ZP$	Predatory zooplankton threshold value for grazing on large phytoplankton	mmolN m^{-3}	0.040^{S}
$ZS2ZP$	Predatory zooplankton threshold value for grazing on small zooplankton	mmolN m^{-3}	0.040^{S}
$ZL2ZP$	Predatory zooplankton threshold value for grazing on large zooplankton	mmolN m^{-3}	0.040^{S}
α_{ZP}	Assimilation efficiency of predatory zooplankton	no dimension	0.7^{S}
β_{ZP}	Growth efficiency of predatory zooplankton	no dimension	0.3^{S}
Mor_{ZP0}	Predatory zooplankton mortality rate at 0 ℃	m^{3} mmolN^{-1} day^{-1}	0.12^{S}
K_{GraP}	Predatory zooplankton temperature coefficient for grazing	℃$^{-1}$	0.0693^{S}

K_{MorZP}	Predatory zooplankton temperature coefficient for mortality	$℃^{-1}$	0.0693[S]
ψ_{PL}	Grazing inhibition coefficient of predatory zooplankton grazing on large phytoplankton	m^3 mmolN^{-1}	4.605[S]
ψ_{ZS}	Grazing inhibition coefficient of predatory zooplankton grazing on small zooplankton	m^3 mmolN^{-1}	3.01[S]
	Light		
$AttSW$	Light attenuation due to seawater	m^{-1}	0.03[S]
$AttPS$	Light attenuation due to small phytoplankton, self-shading coefficient	m^2 mmolN^{-1}	0.03[S]
$AttPL$	Light attenuation due to large phytoplankton, self-shading coefficient	m^2 mmolN^{-1}	0.03[S]
$frac$	Fraction of shortwave radiation that is photosynthetically active	no dimension	0.43[S]
I_0	Threshold of light inhibition of nitrification	W m^{-2}	0.0095[F06]
k_I	Light intensity at which light inhibition of nitrification is half-saturated	W m^{-2}	0.1[F06]
	Water column nitrification and aerobic decomposition		
Nit_0	Nitrification rate at 0 ℃	day^{-1}	0.003[S]
$VP2N_0$	Decomposition rate at 0 ℃ (PON→NH_4)	day^{-1}	0.01[S]
$VP2D_0$	Decomposition rate at 0 ℃ (PON→DON)	day^{-1}	0.05[S]
$VD2N_0$	Decomposition rate at 0 ℃ (DON→NH_4)	day^{-1}	0.02[S]
$VO2S_0$	Decomposition rate at 0 ℃ (Opal→$Si(OH)_4$)	day^{-1}	0.01[S]
K_{Nit}	Temperature coefficient for nitrification	$℃^{-1}$	0.0693[S]
K_{P2D}	Temperature coefficient for decomposition (PON→DON)	$℃^{-1}$	0.0693[S]
K_{P2N}	Temperature coefficient for decomposition (PON→NH_4)	$℃^{-1}$	0.0693[S]
K_{D2N}	Temperature coefficient for decomposition (DON→NH_4)	$℃^{-1}$	0.0693[S]

K_{O2S}	Temperature coefficient for decomposition (Opal→$Si(OH)_4$)	$℃^{-1}$	0.0693[S]
Other parameters			
K_{Oxyg}	Oxygen concentration at which inhibition of nitrification and aerobic respiration are half-saturated	mmolO_2 m^{-3}	3.0[F13]
$Oxyg_{th}$	Oxygen concentration threshold below which no aerobic respiration or nitrification occurs	mmolO_2 m^{-3}	6.0[F13]
$RPO4N$	P: N ratio	mmolP mmolN^{-1}	1/16[L]
$RSiN$	Si: N ratio	mmolSi mmolN^{-1}	1[S]
$rOxNO_3$	Stoichiometric ratios corresponding to the oxygen produced per mol of nitrate assimilated during photosynthesis	mmolO_2 mmolNO_3^{-1}	138/16[F13]
$rOxNH_4$	Stoichiometric ratios corresponding to the oxygen produced per mol of ammonium assimilated during photosynthesis	mmolO_2 mmolNH_4^{-1}	106/16[F13]
$setVPON$	Sinking velocity of PON	m day^{-1}	-5*
$setVOpal$	Sinking velocity of Opal	m day^{-1}	-5*

Appendix C: Supporting figures

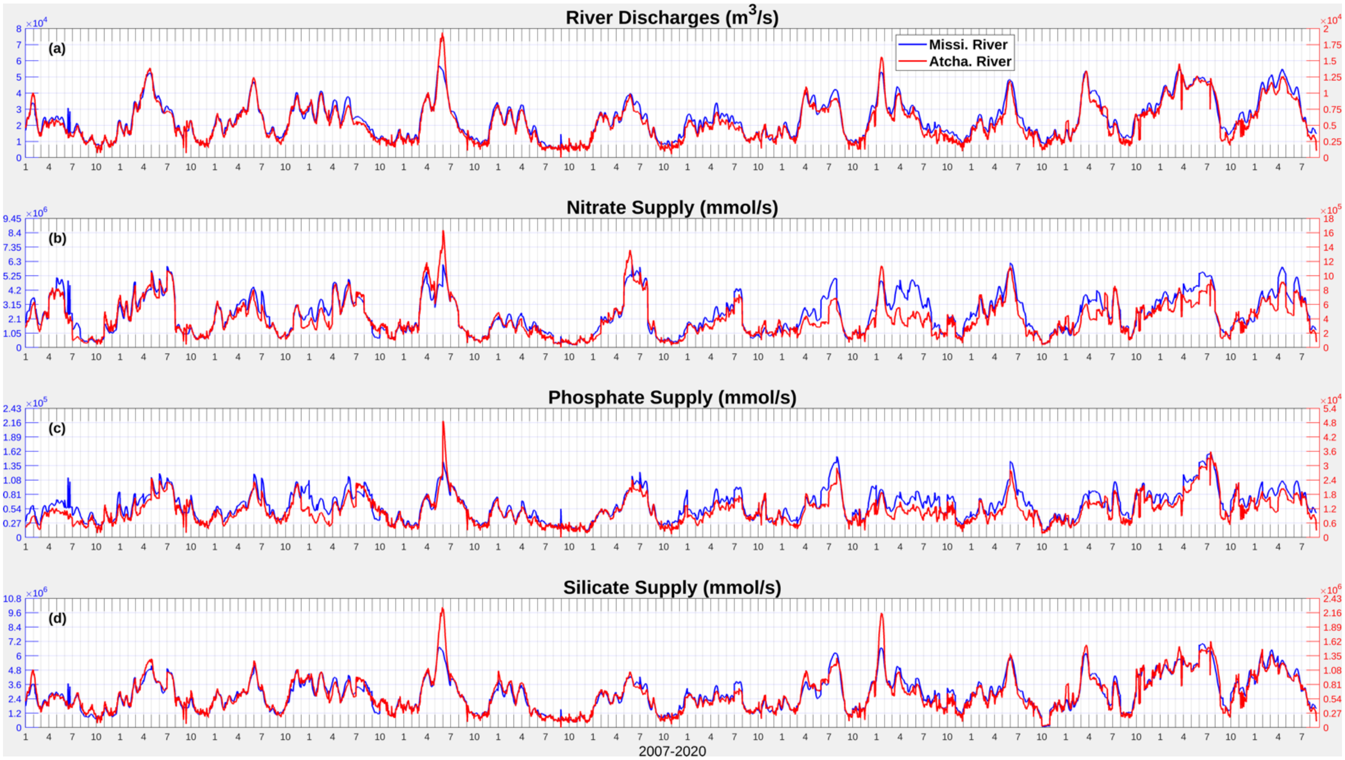

Figure C1. Daily time series (2007–2020) of river discharges of freshwater, nitrate, phosphate, and silicate from the Mississippi and Atchafalaya rivers.

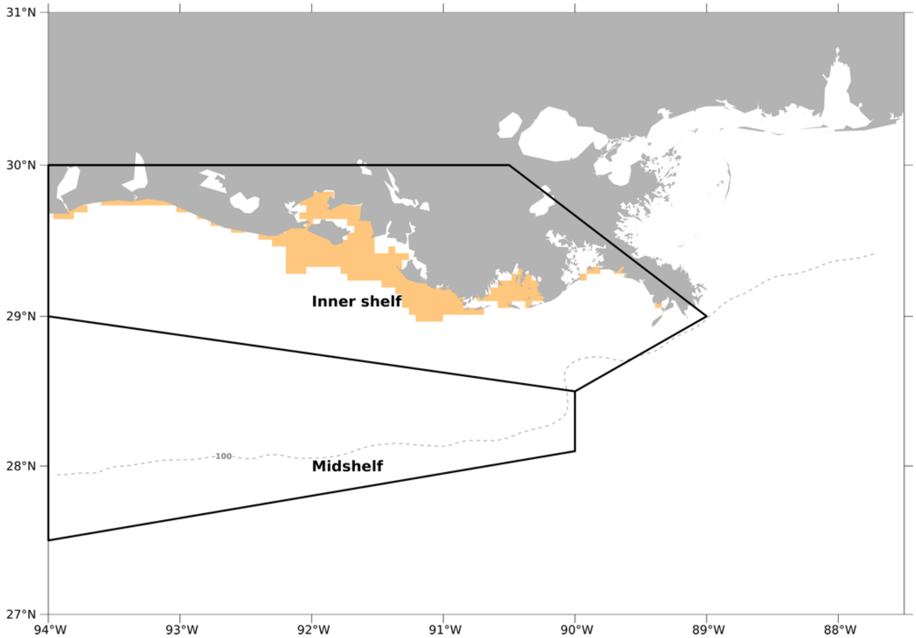

Figure C2. The model computational meshes over which the regionally averaged diatom ratios were conducted for validation purposes. The orange-patched region covers roughly the study regions in Schaeffer et al. (2012), while the regions restricted by two black polygons are two regions (i.e., inner shelf and mid shelf) where samples were collected in Chakraborty and Lohrenz's (2015) study.

References

Anglès, S., Jordi, A., Henrichs, D. W., and Campbell, L.: Influence of coastal upwelling and river discharge on the phytoplankton community composition in the northwestern Gulf of Mexico, Prog. Oceanogr., 173, 26–36, https://doi.org/10.1016/j.pocean.2019.02.001, 2019.

Baronas, J. J., Hammond, D. E., Berelson, W. M., McManus, J., and Severmann, S.: Germanium-silicon fractionation in a river-influenced continental margin: The Northern Gulf of Mexico, Geochim. Cosmochim. Acta, 178, 124–142, https://doi.org/10.1016/j.gca.2016.01.028, 2016.

Bianchi, T. S., DiMarco, S. F., Cowan, J. H., Hetland, R. D., Chapman, P., Day, J. W., and Allison, M. A.: The science of hypoxia in the northern Gulf of Mexico: A review, Sci. Total Environ., 408, 1471–1484, https://doi.org/10.1016/j.scitotenv.2009.11.047, 2010.

Bleck, R.: An oceanic general circulation model framed in hybrid isopycnic-Cartesian coordinates, Ocean Model., 4, 55–88, https://doi.org/10.1016/S1463-5003(01)00012-9, 2002.

Bleck, R. and Boudra, D. B.: Initial testing of a numerical ocean circulation model using a hybrid (quasi-isopycnic) vertical coordinate, J. Phys. Oceanogr., 11, 755–770, https://doi.org/https://doi.org/10.1175/1520-0485(1981)011<0755:ITOANO>2.0.CO;2, 1981.

Boyer, T. P., Baranova, O. K., Coleman, C., Garcia, H. E., Grodsky, A., Locarnini, R. A., Mishonov, A. V, Paver, C. R., Reagan, J. R., Seidov, D., Smolyar, I. V, Weathers, K. W., and Zweng, M. M.: World Ocean Database 2018, Technical., edited by: Mishonov, A. V., NOAA Atlas NESDIS 87, 2018.

Chakraborty, S. and Lohrenz, S. E.: Phytoplankton community structure in the river-influenced continental margin of the northern Gulf of Mexico, Mar. Ecol. Prog. Ser., 521, 31–47, https://doi.org/10.3354/meps11107, 2015.

Chakraborty, S., Lohrenz, S. E., and Gundersen, K.: Photophysiological and light absorption properties of phytoplankton communities in the river-dominated margin of the northern Gulf of Mexico, J. Geophys. Res. Ocean., 122, 4922–4938, https://doi.org/10.1002/2016JC012092, 2017.

Chapman, D. C.: Numerical treatment of cross-shelf open boundaries in a barotropic coastal ocean model., https://doi.org/10.1175/1520-0485(1985)015<1060:ntocso>2.0.co;2, 1985.

Cummings, J. A.: Operational multivariate ocean data assimilation, Q. J. R. Meteorol. Soc., 131, 3583–3604, https://doi.org/10.1256/qj.05.105, 2005.

Cummings, J. A. and Smedstad, O. M.: Variational Data Assimilation for the Global Ocean, in: Data Assimilation for Atmospheric, Oceanic and Hydrologic Applications, vol. II, edited by: Park, S. K. and Xu, L., Springer Berlin Heidelberg, 303–343, https://doi.org/10.1007/978-3-642-35088-7_13, 2013.

Feng, Y., Fennel, K., Jackson, G. A., DiMarco, S. F., and Hetland, R. D.: A model study of the response of hypoxia to upwelling-favorable wind on the northern Gulf of Mexico shelf, J. Mar. Syst., 131, 63–73, https://doi.org/10.1016/j.jmarsys.2013.11.009, 2014.

Fennel, K. and Laurent, A.: N and P as ultimate and proximate limiting nutrients in the northern Gulf of Mexico: Implications for hypoxia reduction strategies, 15, 3121–3131, https://doi.org/10.5194/bg-15-3121-2018, 2018.

Fennel, K. and Testa, J. M.: Biogeochemical Controls on Coastal Hypoxia, Ann. Rev. Mar. Sci., 11, 105–130, https://doi.org/10.1146/annurev-marine-010318-095138, 2019.

Fennel, K., Wilkin, J., Levin, J., Moisan, J., O'Reilly, J., and Haidvogel, D.: Nitrogen cycling in the Middle Atlantic Bight: Results from a three-dimensional model and implications for the North Atlantic nitrogen budget, Global Biogeochem. Cycles, 20, 1–14, https://doi.org/10.1029/2005GB002456, 2006.

Fennel, K., Hetland, R., Feng, Y., and Dimarco, S.: A coupled physical-biological model of the Northern Gulf of Mexico shelf: Model description, validation and analysis of phytoplankton variability, 8, 1881–1899, https://doi.org/10.5194/bg-8-1881-2011, 2011.

Fennel, K., Hu, J., Laurent, A., Marta-Almeida, M., and Hetland, R.: Sensitivity of hypoxia predictions for the northern Gulf of Mexico to sediment oxygen consumption and model nesting, J. Geophys. Res. Ocean., 118, 990–1002, https://doi.org/10.1002/jgrc.20077, 2013.

Fennel, K., Laurent, A., Hetland, R., Justic, D., Ko, D. S., Lehrter, J., Murrell, M., Wang, L., Yu, L., and Zhang, W.: Effects of model physics on hypoxia simulations for the northern Gulf of Mexico: A model intercomparison, J. Geophys. Res. Ocean., 121, 5731–5750, https://doi.org/10.1002/2015JC011516, 2016.

Fiechter, J. and Moore, A. M.: Interannual spring bloom variability and Ekman pumping in the coastal Gulf of Alaska, J. Geophys. Res. Ocean., 114, 1–19, https://doi.org/10.1029/2008JC005140, 2009.

Flather, R. A.: A tidal model of the northwest European continental shelf, Mem. la Soc. R. Sci. Liege, 6, 141–164, 1976.

Fox, D. N., Teague, W. J., Barron, C. N., Carnes, M. R., and Lee, C. M.: The Modular Ocean Data Assimilation System (MODAS), J. Atmos. Ocean. Technol., 19, 240–252, https://doi.org/10.1175/1520-0426(2002)019<0240:TMODAS>2.0.CO;2, 2002.

Garcia, H. E., Weathers, K., Paver, C. R., Smolyar, I., Boyer, T. P., Locarnini, R. A., Zweng, M. M., Mishonov, A. V., Baranova, O. K., Seidov, D., and Reagan, J. R.: World Ocean Atlas 2018, Volume 3: Dissolved Oxygen, Apparent Oxygen Utilization, and Oxygen Saturation, Technical., edited by: Mishonov, A. V., NOAA Atlas NESDIS 83, 38 pp., 2018.

Gomez, F. A., Lee, S. K., Liu, Y., Hernandez, F. J., Muller-Karger, F. E., and Lamkin, J. T.: Seasonal patterns in phytoplankton biomass across the northern and deep Gulf of Mexico: A numerical model study, 15, 3561–3576, https://doi.org/10.5194/bg-15-3561-2018, 2018.

Große, F., Fennel, K., and Laurent, A.: Quantifying the Relative Importance of Riverine and Open-Ocean Nitrogen Sources for Hypoxia Formation in the Northern Gulf of Mexico, J. Geophys. Res. Ocean., 5451–5467, https://doi.org/10.1029/2019jc015230, 2019.

Haidvogel, D. B., Arango, H. G., Hedstrom, K., Beckmann, A., Malanotte-Rizzoli, P., and Shchepetkin, A. F.: Model evaluation experiments in the North Atlantic Basin: Simulations in nonlinear terrain-following coordinates, Dyn. Atmos. Ocean., 32, 239–281, https://doi.org/10.1016/S0377-0265(00)00049-X, 2000.

Helber, R. W., Townsend, T. L., Barron, C. N., Dastugue, J. M., and Carnes, M. R.: Validation Test Report for the Improved Synthetic Ocean Profile (ISOP) System, Part I: Synthetic Profile Methods and Algorithm, 2013.

Hetland, R. D. and DiMarco, S. F.: How does the character of oxygen demand control the structure of hypoxia on the Texas-Louisiana continental shelf?, J. Mar. Syst., 70, 49–62, https://doi.org/10.1016/j.jmarsys.2007.03.002, 2008.

Justić, D. and Wang, L.: Assessing temporal and spatial variability of hypoxia over the inner Louisiana-upper Texas shelf: Application of an unstructured-grid three-dimensional coupled hydrodynamic-water quality model, Cont. Shelf Res., 72, 163–179, https://doi.org/10.1016/j.csr.2013.08.006, 2014.

Justić, D., Rabalais, N. N., and Turner, R. E.: Simulated responses of the Gulf of Mexico hypoxia to variations in climate and anthropogenic nutrient loading, J. Mar. Syst., 42, 115–126, https://doi.org/10.1016/S0924-7963(03)00070-8, 2003.

Justić, D., Bierman, V. J. J., Scavia, D., and Hetland, R. D.: Forecasting Gulf's Hypoxia: The Next 50 Years?, 30, 791–801, 2007.

Kishi, M. J., Kashiwai, M., Ware, D. M., Megrey, B. A., Eslinger, D. L., Werner, F. E., Noguchi-Aita, M., Azumaya, T., Fujii, M., Hashimoto, S., Huang, D., Iizumi, H., Ishida, Y., Kang, S., Kantakov, G. A., Kim, H. cheol, Komatsu, K., Navrotsky, V. V., Smith, S. L., Tadokoro, K., Tsuda, A., Yamamura, O., Yamanaka, Y., Yokouchi, K., Yoshie, N., Zhang, J., Zuenko, Y. I., and Zvalinsky, V. I.: NEMURO-a lower trophic level model for the North Pacific marine ecosystem, Ecol. Modell., 202, 12–25, https://doi.org/10.1016/j.ecolmodel.2006.08.021, 2007.

Laurent, A. and Fennel, K.: Simulated reduction of hypoxia in the northern Gulf of Mexico due to phosphorus limitation, Elem. Sci. Anthr., 2, 1–12, https://doi.org/10.12952/journal.elementa.000022, 2014.

Laurent, A. and Fennel, K.: Time-Evolving, Spatially Explicit Forecasts of the Northern Gulf of Mexico Hypoxic Zone, Environ. Sci. Technol., 53, 14449–14458, https://doi.org/10.1021/acs.est.9b05790, 2019.

Laurent, A., Fennel, K., Hu, J., and Hetland, R.: Simulating the effects of phosphorus limitation in the Mississippi and Atchafalaya river plumes, 9, 4707–4723, https://doi.org/10.5194/bg-9-4707-2012, 2012.

Laurent, A., Fennel, K., Wilson, R., Lehrter, J., and Devereux, R.: Parameterization of biogeochemical sediment-water fluxes using in situ measurements and a diagenetic model, 13, 77–94, https://doi.org/10.5194/bg-13-77-2016, 2016.

Laurent, A., Fennel, K., Ko, D. S., and Lehrter, J.: Climate change projected to exacerbate impacts of coastal Eutrophication in the Northern Gulf of Mexico, J. Geophys. Res. Ocean., 123, 3408–3426, https://doi.org/10.1002/2017JC013583, 2018.

Li, Q. P., Franks, P. J. S., Landry, M. R., Goericke, R., and Taylor, A. G.: Modeling phytoplankton growth rates and chlorophyll to carbon ratios in California coastal and pelagic ecosystems, J. Geophys. Res. Biogeosciences, 115, 1–12, https://doi.org/10.1029/2009JG001111, 2010.

Marchesiello, P., McWilliams, J. C., and Shchepetkin, A.: Open boundary conditions for long-term integration of regional oceanic models, Ocean Model., 3, 1–20, https://doi.org/10.1016/S1463-5003(00)00013-5, 2001.

Mattern, J. P., Fennel, K., and Dowd, M.: Sensitivity and uncertainty analysis of model hypoxia estimates for the Texas-Louisiana shelf, J. Geophys. Res. Ocean., 118, 1316–1332, https://doi.org/10.1002/jgrc.20130, 2013.

McCarthy, M. J., Carini, S. A., Liu, Z., Ostrom, N. E., and Gardner, W. S.: Oxygen consumption in the water column and sediments of the northern Gulf of Mexico hypoxic zone, Estuar. Coast. Shelf Sci., 123, 46–53, https://doi.org/10.1016/j.ecss.2013.02.019, 2013.

Mississippi River/Gulf of Mexico Watershed Nutrient Task Force: Action Plan for Reducing, Mitigating, and Controlling Hypoxia in the Northern Gulf of Mexico, Washington,DC., 2001.

Mississippi River/Gulf of Mexico Watershed Nutrient Task Force: Gulf Hypoxia Action Plan 2008 for Reducing, Mitigating, and Controlling Hypoxia in the Northern Gulf of Mexico and Improving Water Quality in the Mississippi River Basin, Washington,DC., 2008.

Moriarty, J. M., Harris, C. K., Friedrichs, M. A. M., Fennel, K., and Xu, K.: Impact of Seabed Resuspension on Oxygen and Nitrogen Dynamics in the Northern Gulf of Mexico: A Numerical Modeling Study, J. Geophys. Res. Ocean., 123, 7237–7263, https://doi.org/10.1029/2018JC013950, 2018.

Murrell, M. C. and Lehrter, J. C.: Sediment and Lower Water Column Oxygen Consumption in the Seasonally Hypoxic Region of the Louisiana Continental Shelf, 34, 912–924, https://doi.org/10.1007/s12237-010-9351-9, 2011.

Obenour, D. R., Michalak, A. M., and Scavia, D.: Assessing biophysical controls on Gulf of Mexico hypoxia through probabilistic modeling, Ecol. Appl., 25, 492–505, https://doi.org/10.1890/13-2257.1, 2015.

Olson, R. J.: Differential photoinhibition of marine nitrifying bacteria: a possible mechanism for the formation of the primary nitrite maximum, J. Mar. Res., 39, 227–238, 1981.

Parker, R. A.: Dynamic models for ammonium inhibition of nitrate uptake by phytoplankton, Ecol. Modell., 66, 113–120, https://doi.org/10.1016/0304-3800(93)90042-Q, 1993.

Platt, T., Gallegos, C. L., and Harrison, W. G.: Photoinhibition of photosynthesis in natural assemblages of marine phytoplankton, J. Mar. Res., 38, 687–701, 1980.

Rabalais, N. N. and Baustian, M. M.: Historical Shifts in Benthic Infaunal Diversity in the Northern Gulf of Mexico since the Appearance of Seasonally Severe Hypoxia, 12, https://doi.org/10.3390/d12020049, 2020.

Rabalais, N. N. and Turner, R. E.: Gulf of Mexico Hypoxia: Past, Present, and Future, Limnol. Oceanogr. Bull., 28, 117–124, https://doi.org/10.1002/lob.10351, 2019.

Rabalais, N. N., Turner, R. E., and Wiseman, W. J.: Gulf of Mexico hypoxia, a.k.a. "The dead zone," Annu. Rev. Ecol. Syst., 33, 235–263, https://doi.org/10.1146/annurev.ecolsys.33.010802.150513, 2002.

Rabalais, N. N., Turner, R. E., Sen Gupta, B. K., Boesch, D. F., Chapman, P., and Murrell, M. C.: Hypoxia in the northern Gulf of Mexico: Does the science support the plan to reduce, mitigate, and control hypoxia?, 30, 753–772, https://doi.org/10.1007/BF02841332, 2007a.

Rabalais, N. N., Turner, R. E., Gupta, B. K. S., Platon, E., and Parsons, M. L.: Sediments tell the history of eutrophication and hypoxia in the northern Gulf of Mexico, Ecol. Appl., 17, 129–143, https://doi.org/10.1890/06-0644.1, 2007b.

Rowe, G. T., Cruz Kaegi, M. E., Morse, J. W., Boland, G. S., and Escobar Briones, E. G.: Sediment community metabolism associated with continental shelf hypoxia, northern Gulf of Mexico, 25, 1097–1106, https://doi.org/10.1007/BF02692207, 2002.

Ruiz Xomchuk, V., Hetland, R. D., and Qu, L.: Small-Scale Variability of Bottom Oxygen in the Northern Gulf of Mexico, https://doi.org/10.1029/2020JC016279, 2021.

Saha, S., Moorthi, S., Pan, H.-L., Wu, X., Wang, J., Nadiga, S., Tripp, P., Kistler, R., Woollen, J., Behringer, D., Liu, H., Stokes, D., Grumbine, R., Gayno, G., Wang, J., Hou, Y.-T., Chuang, H.-Y., Juang, H.-M. H., Sela, J., Iredell, M., Treadon, R., Kleist, D., Van Delst, P., Keyser, D., Derber, J., Ek, M., Meng, J., Wei, H., Yang, R., Lord, S., van den Dool, H., Kumar, A., Wang, W., Long, C., Chelliah, M., Xue, Y., Huang, B., Schemm, J.-K., Ebisuzaki, W., Lin, R., Xie, P., Chen, M., Zhou, S., Higgins, W., Zou, C.-Z., Liu, Q., Chen, Y., Han, Y., Cucurull, L., Reynolds, R. W., Rutledge, G., and Goldberg, M.: NCEP Climate Forecast System Reanalysis (CFSR) 6-hourly Products, January 1979 to December 2010, https://doi.org/10.5065/D69K487J, 2010.

Saha, S., Moorthi, S., Wu, X., Wang, J., Nadiga, S., Tripp, P., Behringer, D., Hou, Y.-T., Chuang, H., Iredell, M., Ek, M., Meng, J., Yang, R., Mendez, M. P., van den Dool, H., Zhang, Q., Wang, W., Chen, M., and Becker, E.: NCEP Climate Forecast System Version 2 (CFSv2) 6-hourly Products, https://doi.org/10.5065/D61C1TXF, 2011.

Scavia, D., Evans, M. A., and Obenour, D. R.: A scenario and forecast model for gulf of mexico hypoxic area and volume, Environ. Sci. Technol., 47, 10423–10428, https://doi.org/10.1021/es4025035, 2013.

Schaeffer, B. A., Kurtz, J. C., and Hein, M. K.: Phytoplankton community composition in nearshore coastal waters of Louisiana, Mar. Pollut. Bull., 64, 1705–1712, https://doi.org/10.1016/j.marpolbul.2012.03.017, 2012.

Seitzinger, S. P. and Giblin, A. E.: Estimating denitrification in North Atlantic continental shelf sediments, in: Nitrogen Cycling in the North Atlantic Ocean and its Watersheds, edited by: Howarth, R. W., Springer Dordrecht, 235–260, https://doi.org/10.1007/978-94-009-1776-7_7, 1996.

Shchepetkin, A. F. and McWilliams, J. C.: The regional oceanic modeling system (ROMS): A split-explicit, free-surface, topography-following-coordinate oceanic model, Ocean Model., 9, 347–404, https://doi.org/10.1016/j.ocemod.2004.08.002, 2005.

Shchepetkin, A. F. and McWilliams, J. C.: Correction and commentary for "Ocean forecasting in terrain-following coordinates: Formulation and skill assessment of the regional ocean modeling system" by Haidvogel et al., J. Comp. Phys. 227, pp. 3595-3624, J. Comput. Phys., 228, 8985–9000, https://doi.org/10.1016/j.jcp.2009.09.002, 2009.

Shropshire, T., Morey, S., Chassignet, E., Bozec, A., Coles, V., Landry, M., Swalethorp, R., Zapfe, G., and Stukel, M.: Quantifying spatiotemporal variability in zooplankton dynamics in the Gulf of Mexico with a physical-biogeochemical model, 17, 3385–3407, https://doi.org/10.5194/bg-17-3385-2020, 2020.

Simpson, J. H.: The shelf-sea fronts: implications of their existence and behaviour, Philos. Trans. R. Soc. London. Ser. A, Math. Phys. Sci., 302, 531–546, https://doi.org/10.1098/rsta.1981.0181, 1981.

Simpson, J. H. and Bowers, D.: Models of stratification and frontal movement in shelf seas, Deep Sea Res. Part A, Oceanogr. Res. Pap., 28, 727–738, https://doi.org/10.1016/0198-0149(81)90132-1, 1981.

Simpson, J. H. and Hunter, J. R.: Fronts in the Irish Sea, Nature, 250, 404–406, https://doi.org/10.1038/250404a0, 1974.

Simpson, J. H., Allen, C. M., and Morris, N. C. G.: Fronts on the Continental Shelf, J. Geophys. Res., 83, 4607–4614, https://doi.org/10.1029/JC083iC09p04607, 1978.

Sylvan, J. B., Quigg, A., Tozzi, S., and Ammerman, J. W.: Eutrophication-induced phosphorus limitation in the Mississippi River plume: Evidence from fast repetition rate fluorometry, Limnol. Oceanogr., 52, 2679–2685, https://doi.org/10.4319/lo.2007.52.6.2679, 2007.

Turner, R. E., Rabalais, N. N., and Justić, D.: Predicting summer hypoxia in the northern Gulf of Mexico: Redux, Mar. Pollut. Bull., 64, 319–324, https://doi.org/10.1016/j.marpolbul.2011.11.008, 2012.

Wang, L. and Justić, D.: A modeling study of the physical processes affecting the development of seasonal hypoxia over the inner Louisiana-Texas shelf: Circulation and stratification, Cont. Shelf Res., 29, 1464–1476, https://doi.org/10.1016/j.csr.2009.03.014, 2009.

Wanninkhof, R.: Relationship Between Wind Speed and Gas Exchange Over the Ocean, J. Geophys. Res., 97, 7373–7382, https://doi.org/10.1029/92JC00188, 1992.

Warner, J. C., Geyer, W. R., and Lerczak, J. A.: Numerical modeling of an estuary: A comprehensive skill assessment, J. Geophys. Res. C Ocean., 110, 1–13, https://doi.org/10.1029/2004JC002691, 2005.

Warner, J. C., Armstrong, B., He, R., and Zambon, J. B.: Development of a Coupled Ocean-Atmosphere-Wave-Sediment Transport (COAWST) Modeling System, Ocean Model., 35, 230–244, https://doi.org/10.1016/j.ocemod.2010.07.010, 2010.

Warner, J. C., Defne, Z., Haas, K., and Arango, H. G.: A wetting and drying scheme for ROMS, Comput. Geosci., 58, 54–61, https://doi.org/10.1016/j.cageo.2013.05.004, 2013.

Wawrik, B. and Paul, J. H.: Phytoplankton community structure and productivity along the axis of the Mississippi River plume in oligotrophic Gulf of Mexico waters, Aquat. Microb. Ecol., 35, 185–196, https://doi.org/10.3354/ame035185, 2004.

Yu, L., Fennel, K., and Laurent, A.: A modeling study of physical controls on hypoxia generation in the northern Gulf of Mexico, J. Geophys. Res. Ocean., 120, 5019–5039, https://doi.org/10.1002/ 2014JC010634, 2015.

Zang, Z., Xue, Z. G., Bao, S., Chen, Q., Walker, N. D., Haag, A. S., Ge, Q., and Yao, Z.: Numerical study of sediment dynamics during hurricane Gustav, Ocean Model., 126, 29–42, https://doi.org/10.1016/j.ocemod.2018.04.002, 2018.

Zang, Z., Xue, Z. G., Xu, K., Bentley, S. J., Chen, Q., D'Sa, E. J., and Ge, Q.: A Two Decadal (1993–2012) Numerical Assessment of

Sediment Dynamics in the Northern Gulf of Mexico, 11, 938, https://doi.org/10.3390/w11050938, 2019.

Zang, Z., Xue, Z. G., Xu, K., Ozdemir, C. E., Chen, Q., Bentley, S. J., and Sahin, C.: A Numerical Investigation of Wave-Supported Gravity Flow During Cold Fronts Over the Atchafalaya Shelf, J. Geophys. Res. Ocean., 125, 1–24, https://doi.org/10.1029/2019JC015269, 2020.